

NASA Technical Memorandum 4566
ATCOM Technical Report 94-A-013

Navier-Stokes and Potential Theory Solutions for a Helicopter Fuselage and Comparison With Experiment

Mark S. Chaffin
ViGYAN, Inc. • Hampton, Virginia

John D. Berry
Langley Research Center • Hampton, Virginia

National Aeronautics and Space Administration
Langley Research Center • Hampton, Virginia 23681-0001

June 1994

The use of trademarks or names of manufacturers in this report is for accurate reporting and does not constitute an official endorsement, either expressed or implied, of such products or manufacturers by the National Aeronautics and Space Administration.

Summary

Two computational methods are used to predict the flow over a generic helicopter fuselage of a simple configuration. A thin-layer Navier-Stokes code and a panel method code are used to compute the surface pressures for comparison with data from 4 experimental conditions at 14 fuselage stations. The findings of both methods are in agreement with the experimental pressure data. However, separation patterns and other viscous flow features from the Navier-Stokes code solution are shown that cannot be easily modeled with the panel method.

Symbols

a	speed of sound, ft/sec
C_p	pressure coefficient, $\frac{p-p_\infty}{q_\infty}$
l	fuselage length, 10.328 ft
M_∞	Mach number, $\frac{V}{a}$
p	pressure, lb/ft ²
q	dynamic pressure, $\frac{1}{2}\rho V^2$, lb/ft ²
R	helicopter rotor radius, 5.164 ft
N_{Re}	Reynolds number, $\frac{Vl}{\nu}$
V	free-stream velocity, ft/sec
X, Y, Z	Cartesian coordinates, ft (fig. 1)
α	angle of attack
ρ	fluid density, slugs/ft ³
ν	kinematic viscosity, ft ² /sec
ξ, η, ζ	curvilinear coordinates (fig. 2)

Introduction

Given the wide range of flight conditions in which helicopters must operate, particularly during hovering maneuvers, and given design constraints based on internal cargo and external stores, the aerodynamic optimization of the fuselage is not always possible. However, the fuselage can significantly affect the overall performance of the helicopter in all flight conditions. Understanding and predicting the aerodynamics of helicopter fuselages will be important to future designs, particularly when the designs require greater range and speed.

Analytical methods for evaluating the aerodynamics of helicopter fuselages are available, including both potential theory and Navier-Stokes solutions. Early computational methods such as in

reference 1 were based on the solution of the potential equation using a singularity method with constant-strength source panels. Since that early work, the computation of flow over arbitrarily shaped bodies has advanced significantly. Many examples of the extent to which panel methods have advanced can be found in reference 2.

The shape of most helicopter fuselages as well as the wide range of flight conditions virtually guarantees that some amount of flow separation will occur. A computational method could model this separation in panel methods with a boundary layer model (coupled inviscid and viscous solver). However, if separation does occur, the code must also model the wake. This modeling is done by shedding a wake that convects downstream the vorticity released when the boundary layer separates. The success of this approach depends on the ability to correctly calculate both where the wake leaves the fuselage and its trajectory. One approach is to test the configuration in a wind tunnel and determine the separation location experimentally. This information can then be used in the potential code to determine the wake location. (See refs. 3 and 4.) More sophisticated approaches determine the wake separation point as part of the boundary layer solution. (See ref. 5.) Although much has been done to improve potential methods for computing separation, the calculation of helicopter fuselage flows remains challenging.

New methods are becoming available that promise better predictions of complex helicopter fuselage flows, particularly of separation. The Navier-Stokes equations are the basis for computing the flow in complex separation regions. In the past several years, much progress has been made in the solution methods needed to solve the Navier-Stokes equations. Applications of thin-layer Navier-Stokes solvers to airfoils and wings can be found in references 6 and 7. In reference 8, solutions are shown for low-speed conditions over a prolate spheroid. However, few references are available that demonstrate the calculation of flow over a helicopter fuselage. Narramore and Brand (ref. 9) used a thin-layer Navier-Stokes code to study the flow over the fuselage of a Bell 214ST helicopter and made comparisons with experimental results.

This paper uses experimental data from a generic helicopter fuselage shape (ref. 10) to assess these two methods of computation. The data used in this study were obtained at a Mach number of 0.062 and an effective Reynolds number of 4.46×10^6 at angles of attack of -10° , -5° , 0° , and 5° . By computing the flow over this fuselage at these angles of attack and by comparing both pressure distributions and

flow features, we will summarize the strengths and weaknesses of these two methods for predicting this flow.

Codes

The two computational methods used for this study represent different approaches to the modeling of fluid flow. The first method, the VSAERO code (ref. 11), uses potential theory with a boundary layer calculation coupled with the inviscid solution. The second method, the CFL3D code (ref. 8), solves the thin-layer Navier-Stokes equations. Both methods allow the study of separation and vortical flow; however, the potential-theory code requires empirical knowledge of the separation and the Navier-Stokes method computes separation from first principles.

The VSAERO code is a commercially available potential-theory panel-method code capable of computing flow over bodies of arbitrary shape. The body is represented by panels on which the source and doublet strengths are determined. Two-dimensional boundary layer calculations can be made along surface streamlines. The effects of the boundary layer calculations can then be coupled with the potential-theory solution. Wake panels can be used to simulate separation (e.g., behind bluff bodies or at the trailing edges of wings). The boundary layer calculation will indicate where separation will occur; however, the user is responsible for determining the starting location of the wakes. Iterations can then be performed on the wakes to allow them to deform to equilibrium. Advantages of the code include speed, ability to represent complex geometries, and ease of use. However, modeling separation (e.g., behind bluff bodies) can be difficult.

The CFL3D code was developed at NASA Langley Research Center and solves the thin-layer Navier-Stokes equations. The code uses a third-order upwind-biased method with Roe flux-difference splitting to solve the equations. A multigrid scheme is used to improve the convergence time. The code is also capable of using multiblock grids, although for this study a single-block grid was used. Turbulence is modeled after the approaches of Baldwin and Lomax. (See ref. 12.) The cases presented here involve some amounts of separation where the Baldwin-Lomax model is uncertain (ref. 13); however, during these calculations this turbulence model was the only one available.

Geometry

The geometry chosen for this study was the rotor body interaction fuselage (ROBIN) that has

been used in several helicopter investigations in the Langley 14- by 22-Foot Subsonic Wind Tunnel. (See ref. 13.) Figure 1 shows a computer simulation of the top and side views of this fuselage, the pressure tap locations used in a specific test, and the model itself installed in the tunnel. This body is defined analytically so easy refinements can be made to the geometry during grid development. Experimental data are available in the form of steady pressures at 14 stations along the fuselage. The data given are for the fuselage with the rotor hub but with the blades removed. No attempt was made to model the rotor hub in any of the calculations.

A C-O volume grid was used for the configuration and is shown with the surface grid in figure 2. Several grid refinements were used to obtain the proper definition of the fuselage for the Navier-Stokes code. These refinements altered the distribution of the surface grid to reduce the solution dependency on the grid. The final volume grid consisted of 145 points in the streamwise direction, 65 radial points, and 65 points in the normal direction. The surface grid consisted of 129 streamwise points and 65 radial points.

The Gridgen code (ref. 14) was used to generate a single-block grid for these calculations. A single-block grid was chosen because future pilot Navier-Stokes codes may not handle multiblock grids. However, a single-block grid makes the generation of a surface grid difficult, primarily at the intersection of the nacelle and the fuselage. The nose and tail regions of the nacelle cause disturbances in the surface grid that affect the gridding on the rest of the fuselage with the Gridgen algorithm used. The solution to this problem was to cluster the streamwise grid lines that make up the nacelle in a narrow region ahead of and behind the nacelle. (See the detail in fig. 2.) This change in grid spacing can cause convergence problems due to the abrupt change in grid cell spacing, but it allows the surface of the nacelle to be accurately defined.

The surface grid taken from the volume grid was used to determine the paneling for the VSAERO code. Grid lines were removed from the surface grid to obtain a coarser panel geometry. The final representation contained 1768 panels. Even with this rather coarse surface grid, the VSAERO code panel distribution was much finer than is typically required to resolve the flow for this type of geometry.

Results

All calculations were performed at the experimental Mach number of 0.062. Slow convergence was evident with the Navier-Stokes code. The CFL3D code

was run on the Langley Cray-2 supercomputer. Several central processing unit hours were required to complete the approximately 10 000 iterations needed for a converged solution. Convergence was determined from the plotted evolution of forces. In contrast, the VSAERO code calculations with streamline, boundary layer, and wake calculations required approximately 2 hours on a Silicon Graphics 320VGX workstation. This time depended upon the number of wake and boundary layer iterations required for the forces to converge.

For the VSAERO code calculations, a wake was shed from the tail of the fuselage. Attempts to shed a wake from the back of the nacelle (an area where separation was expected to occur) did not give acceptable results. The location of this wake was determined by estimating a separation line on the nacelle. The main difficulty was the tendency of the wake to pass through the fuselage while it was being relaxed. Alternatively, the wake could be kept rigid; however, the complex flow in this region could make a guess about wake geometry misleading. Thus, results from the region behind the nacelle are unlikely to compare well with the experiment or with the Navier-Stokes solutions.

In reference 10, eight experimental rotor-off cases were presented. Four angles of attack at two different free-stream flow conditions were studied. For this study, comparisons were made only with the low-speed cases, primarily to reduce the cost of the calculations. Experimental pressures at 14 stations are available for each case. Figures 3-6 show comparisons between experiment and theory. Test conditions and pressure locations for these figures are given in table I.

Pressure

Figure 3 shows the results for the fuselage at an angle of attack of -10° . The pressure coefficient is plotted along the ordinate and the abscissa represents the vertical coordinate of the fuselage surface. The individual plots represent different longitudinal stations along the fuselage.

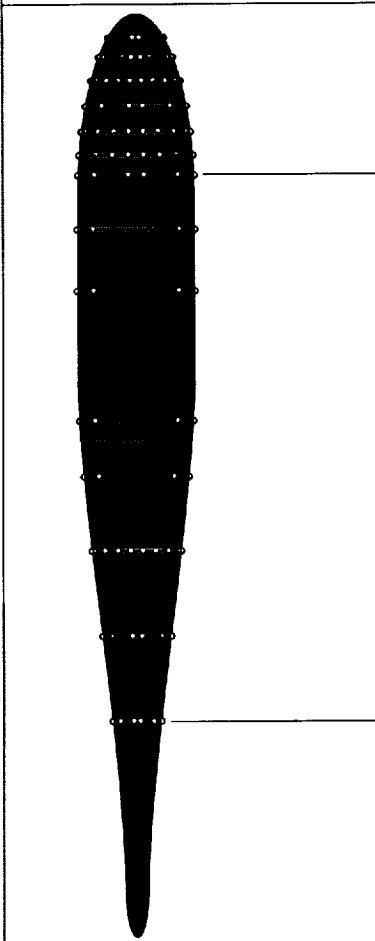
Initially, both codes compare reasonably well with the experiment at most stations. An examination of the stations where separation is expected (figs. 3(k)-3(n)) reveals the advantage of the Navier-Stokes solution. At station $X/R = 1.0008$ (fig. 3(k)), the CFL3D code predicts the separation for $Z/R > 0.12$ (the region behind the nacelle). Because it is a potential-theory code and because this region was not modeled with a wake, the VSAERO code calculates this area as a stagnation region. Thus, we expect

Table I. Index to Test Conditions

(a) Correlation of angle of attack to figures 3-6

Angle of attack	-10°	-5°	0°	5°
Figure	3	4	5	6

(b) Correlation of pressure locations to figures 3-6

Pressure tap locations	X/R	Part of figure
	0.0517	a
	0.0941	b
	0.1450	c
	0.2007	d
	0.2563	e
	0.3074	f
	0.3497	g
	0.4669	h
	0.6003	i
	0.8809	j
	1.0008	k
	1.1620	l
	1.3450	m
	1.5298	n

the pressure rise shown in figure 3(k). A comparison of the last three stations (figs. 3(l)-3(n)) shows the two codes are similarly accurate, except at the bottom of the fuselage. Because of the negative angle of attack and because of the flow disruption due to model installation (fig. 1), some separation might be expected along the bottom centerline of the fuselage. The experimental pressure coefficient begins to approach 0 at this location, as do the results for the CFL3D code. The VSAERO code shows a pressure rise that is characteristic of stagnated flow.

Figure 4 shows the results for the fuselage at an angle of attack of -5° . This case shows a small difference in predicted pressure between the two codes in the region ahead of the nacelle that is not seen at the other angles of attack. In this region, the VSAERO code prediction is closer to the experimental pressure than the CFL3D code. For stations at $X/R \geq 1.0008$ (figs. 4(k)–4(n)), the CFL3D code calculates the surface static pressures more accurately.

Figure 5 shows the results for the fuselage at an angle of attack of 0° . In most cases, the CFL3D code more accurately predicts the experimental pressures than the VSAERO code, especially aft of the nacelle. Again, this difference may relate to the fact that the expected separation from the nacelle was not modeled with the VSAERO code. Another factor that contributes to the discrepancy along the top of the fuselage is the disruption in the flow caused by the wake of the rotor shaft and hub (not modeled by either the panel or Navier-Stokes methods). This factor is most likely to contribute to a discrepancy at both the 0° and 5° angles of attack.

Figure 6 shows the results for the fuselage at an angle of attack of 5° . The results for this case are also similar to the results for the previous cases. However, for this case, the CFL3D code indicates a drop in pressure near the top of the fuselage at stations $X/R > 1.0008$. This drop in pressure is indicative of vortex formation off the fuselage surface. The flow field solution from the CFL3D code can be visualized for confirmation of this vortex.

Flow Features

As part of the postprocessing of the Navier-Stokes results, particle traces were used to study the flow around the fuselage. Particle tracing allows the determination of separation by showing the convergence of streamlines. Particle traces, confined to the layer of the grid adjacent to the surface, simulate what might be seen experimentally with oil flows. The contours of the normalized stagnation pressure were used to study flow characteristics off the fuselage.

Figures 7(a)–7(d) show the normalized stagnation-pressure contours as well as surface streamlines for the four angle-of-attack cases calculated by the CFL3D code. The normalized stagnation-pressure contours can indicate that vortical flow is present; the surface streamlines will show where separation occurs. Figure 7(a) shows the relatively benign flow for the case at -10° . Separation is evident at the back of the nacelle, as expected. From the normalized stagnation-pressure contours, vortical flow is not indicated at the bottom rear of the fuselage. However,

the surface streamlines indicate that a separation line is present along this surface.

The case at -5° is also relatively benign, as shown in figure 7(b). A separation line appears along the lower rear portion of the fuselage that is characteristic of vortical flow. However, the normalized stagnation-pressure contours did not indicate a clear vortex that is shed from the fuselage.

Figure 7(c) shows the case at 0° . A separation line can be seen along the upper rear portion of the fuselage. The normalized stagnation-pressure contours indicate that vortical flow is occurring in this region.

Figure 7(d) shows the results from the CFL3D code for an angle of attack of 5° . On the aft portion of the fuselage, a vortex is shed as evidenced by the normalized stagnation-pressure contours. These contours also show the formation of vortical flow near the intersection of the nacelle and the fuselage as well as a separation line along the upper rear of the fuselage. In previous experimental tests, researchers did not look for these features; therefore, verification is not possible without further experimental measurement.

Calculation of both on- and off-body streamlines is possible with the VSAERO code. The on-body streamlines were calculated and were used for the boundary layer calculation. Boundary layer calculations are performed in a two-dimensional manner along these streamlines; thus, the streamlines will not show the flow deformation that results from the separation on the fuselage. Although the streamlines calculated by the VSAERO code will not show the effect of separation or of vortical flow, they do provide a useful comparison to the Navier-Stokes results.

Surface streamlines calculated by the VSAERO and CFL3D codes are shown for comparison in figures 8(a)–8(d). The results from the VSAERO code do not indicate separation; however, they do allow some understanding of the aerodynamic characteristics of the fuselage. Aside from the differences caused by vortical flow, the main difference in the surface streamlines between the codes seems to occur at locations past the nacelle. This difference is most likely attributable to the ability of the CFL3D code to calculate separation at the rear of the nacelle. Nevertheless, ahead of the nacelle, the two codes agree well.

Conclusions

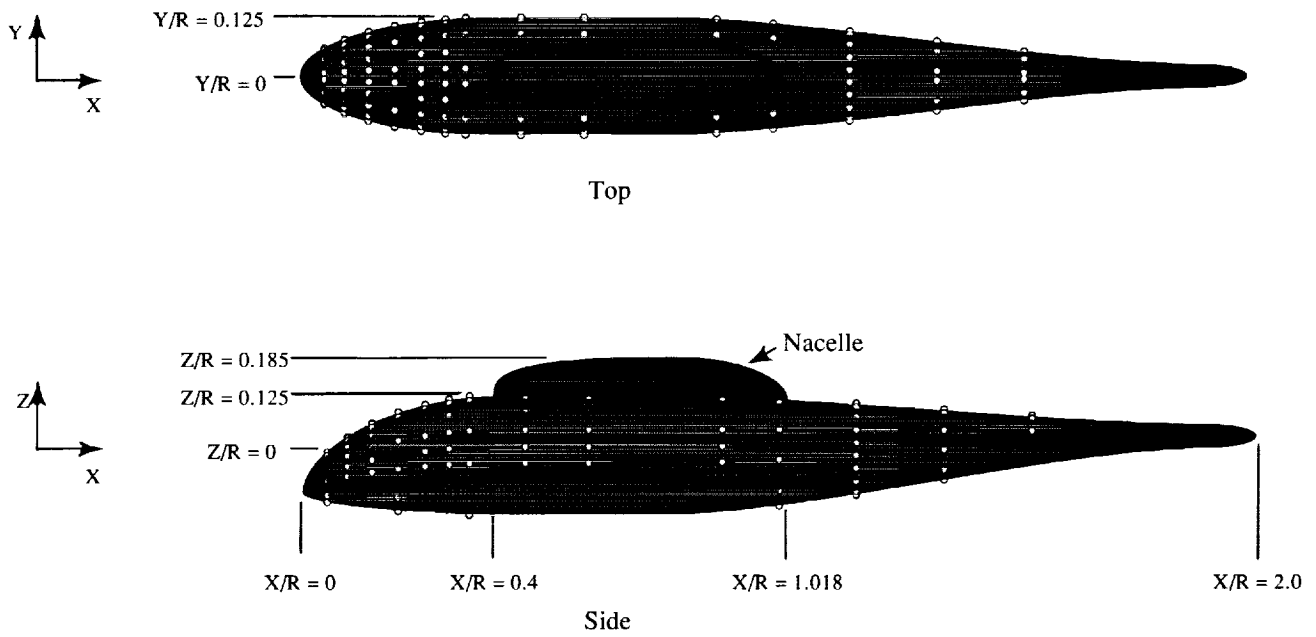
Calculations of the flow properties over a generic helicopter fuselage have been presented and compared with experimental data. Potential-theory and Navier-Stokes methods were used for calculations at

four experimental conditions. Both methods agree well with the experiment. Prediction of flow features such as vortical flow and separation is highlighted. Relatively quick solutions are possible with potential theory, although the ability to calculate regions of separation is unsatisfactory. Although more computationally expensive, the Navier-Stokes method allows separation and vortical flow to be studied from first principles. Although the Navier-Stokes codes predict helicopter fuselage flow sufficiently well for understanding flow characteristics related to viscous properties of the fluid near the body, models for the complex lifting rotor and its wake system must be incorporated for complete characterization of helicopter flows.

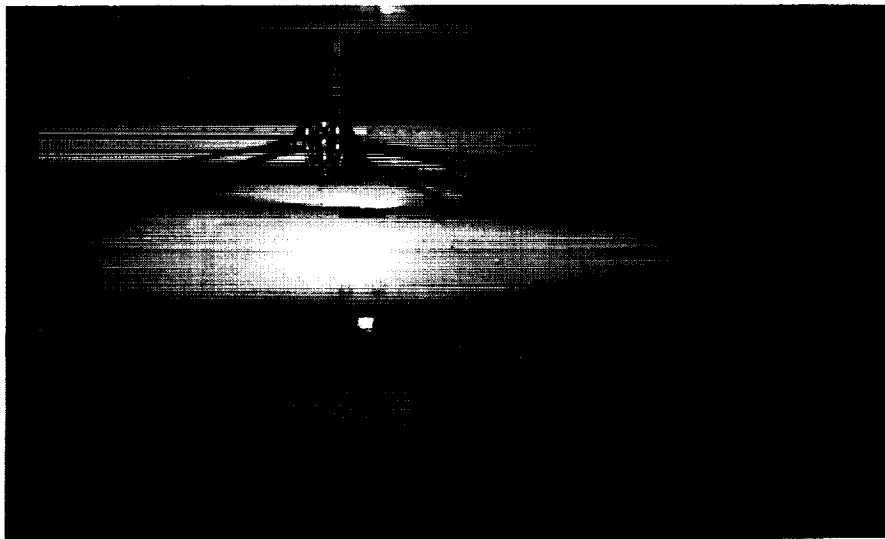
NASA Langley Research Center
Hampton, VA 23681-0001
April 4, 1994

References

1. Hess, John L.; and Smith, A. M. O.: *Calculation of Non-Lifting Potential Flow About Arbitrary Three-Dimensional Bodies*. Rep. No. E.S. 40622 (Contract No. Nonr 2722(00)), Douglas Aircraft Co., Inc., Mar. 15, 1962.
2. Morino L., ed.: *Computational Methods in Potential Aerodynamics*. Springer-Verlag, 1985.
3. Gleyzes, C.; de Saint-Victor, X; and Falempin, G.: Experimental and Numerical Study of the Flow Around an Helicopter Fuselage. Determination of Drag Coefficient. Paper No. 5, *Fifteenth European Rotorcraft Forum*, 1989.
4. Lê, T. H.; Ryan, J.; and Falempin, G.: Wake Modelling for Helicopter Fuselage. Paper no. 2 8, *Thirteenth European Rotorcraft Forum*, 1987.
5. Polz, G. (Leo Kanner Assoc., transl.): *The Calculation of Separated Flow at Helicopter Bodies*. NASA TM-76715, 1982.
6. Bonhaus, Daryl L.; and Wornom, Stephen F.: Comparison of Two Navier-Stokes Codes for Attached Transonic Wing Flows. *J. Aircr.*, vol. 29, no. 1, Jan.-Feb. 1992, pp. 101-107.
7. Maksymiuk, C. M.; Swanson, R. C.; and Pulliam, T. H.: *A Comparison of Two Central Difference Schemes for Solving the Navier-Stokes Equations*. NASA TM-102815, 1990.
8. Vatsa, Veer N.; Thomas, James L.; and Wedan, Bruce W.: Navier-Stokes Computations of Prolate Spheroid at Angle of Attack. *J. Aircr.*, vol. 26, no. 11, Nov. 1989, pp. 986-993.
9. Narramore, J. C.; and Brand, A. G.: Navier-Stokes Correlations to Fuselage Wind Tunnel Test Data. *48th Annual Forum Proceedings*, Volume 1, American Helicopter Soc., June 1992, pp. 447-459.
10. Freeman, Carl E.; and Mineck, Raymond E.: *Fuselage Surface Pressure Measurements of a Helicopter Wind-Tunnel Model With a 3.15-Meter Diameter Single Rotor*. NASA TM-80051, 1979.
11. Maskew, Brian: Prediction of Subsonic Aerodynamic Characteristics: A Case for Low-Order Panel Methods. *J. Aircr.*, vol. 19, no. 2, Feb. 1982, pp. 157-163.
12. Baldwin, Barrett; and Lomax, Harvard: Thin-Layer Approximation and Algebraic Model for Separated Turbulent Flows. AIAA-78-257, Jan. 1978.
13. Maksymiuk, Catherine M.; and Pulliam, Thomas H.: Viscous Transonic Airfoil Workshop Results Using ARC2D. AIAA-87-0415, Jan. 1987.
14. Steinbrenner, John P.; Chawner, John R.; and Fouts, Chris L.: *The Gridgen 3D Multiple Block Grid Generation System—Volume 1: Final Report*. WRDC-TR-90-3022, Vol. 1, U.S. Air Force, July 1990. (Available from DTIC as AD B148 627L.)



(a) Location of pressure taps.



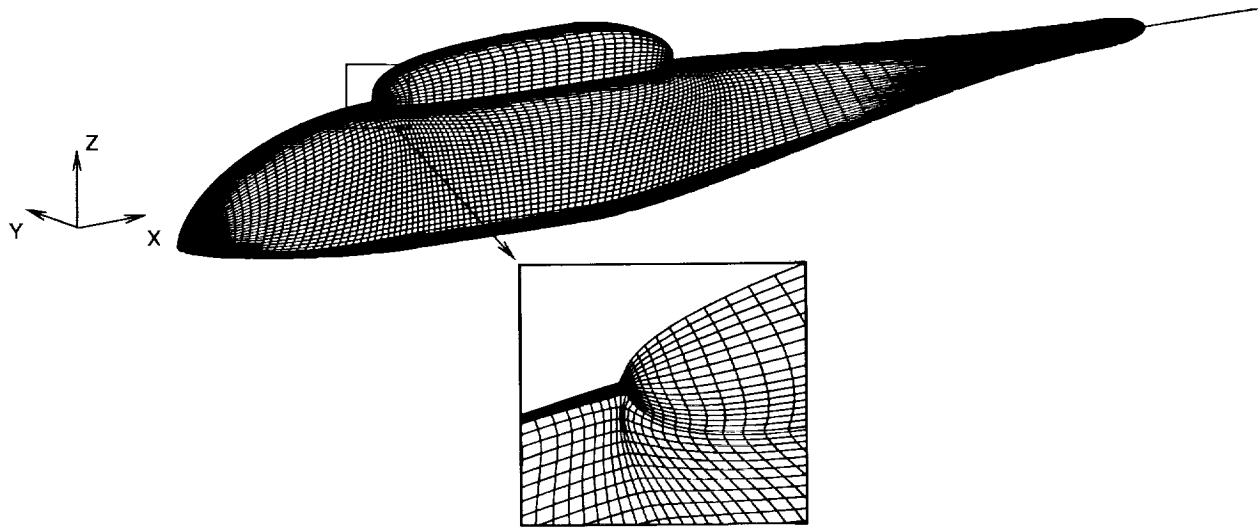
L-78-4383

(b) Model installed in 14- by 22-Foot Subsonic Wind Tunnel.

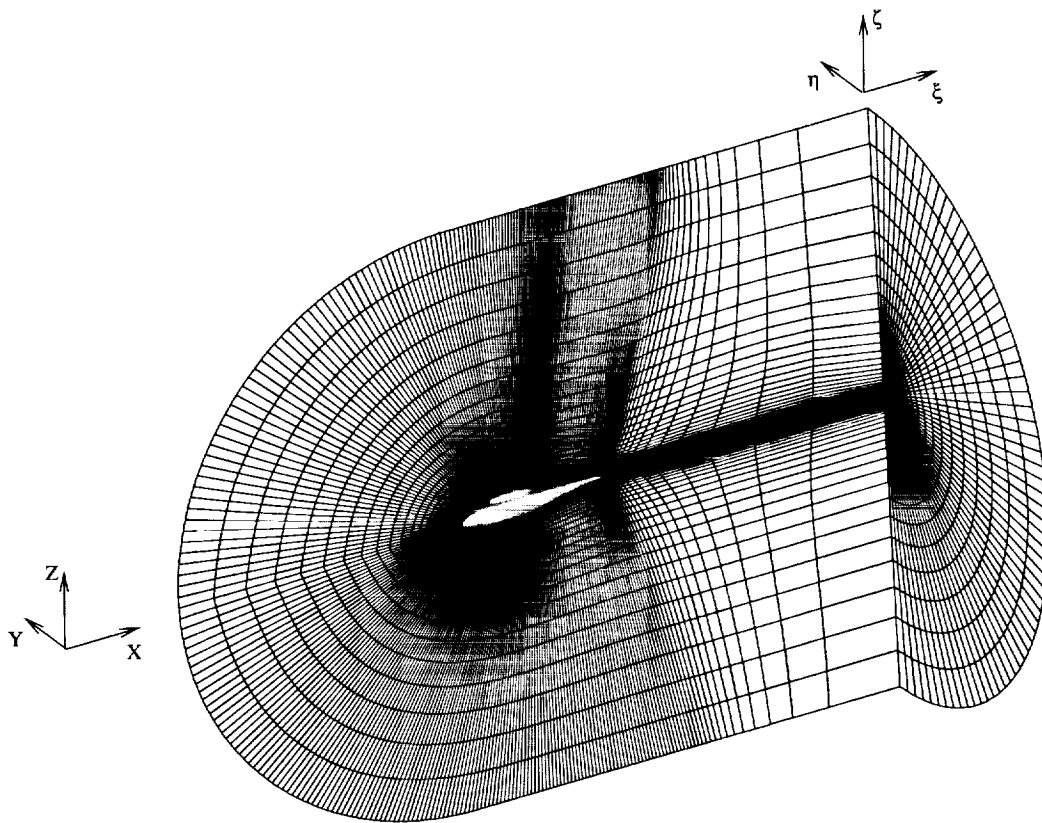
Figure 1. ROBIN fuselage.

ORIGINAL PAGE
BLACK AND WHITE PHOTOGRAPH

~~PRECEDING PAGE DAMAGE NOT REPAIRED~~

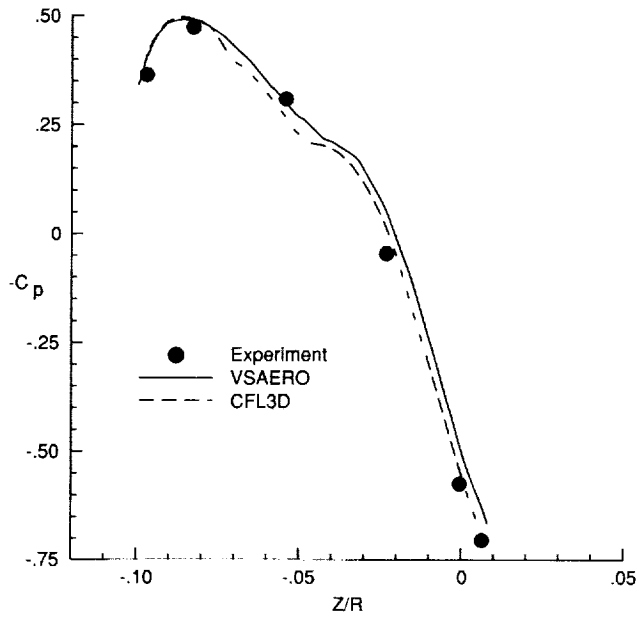


(a) Wire frame surface detail.

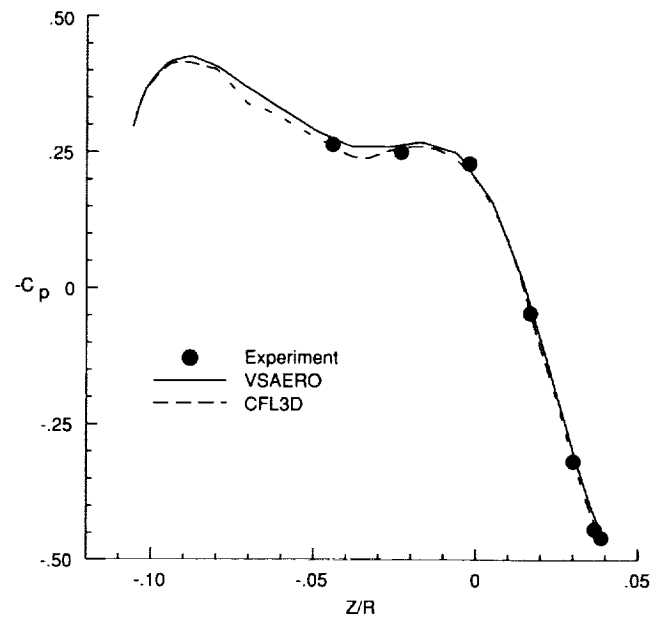


(b) C-O volume grid.

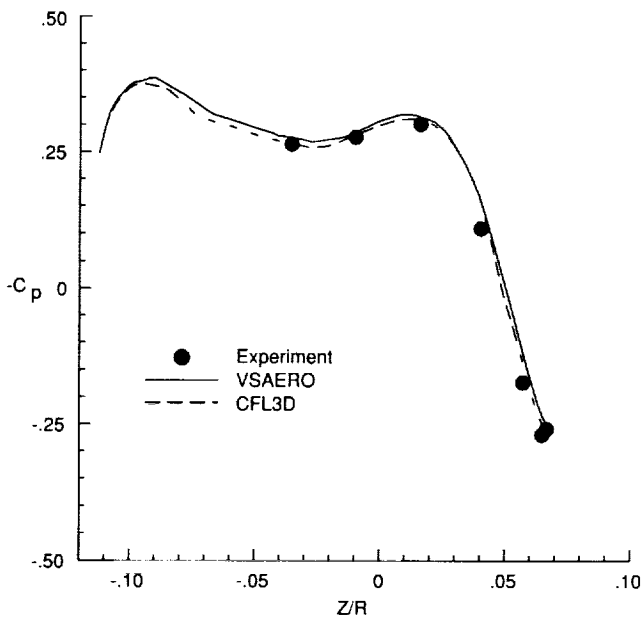
Figure 2. Computational grid for ROBIN.



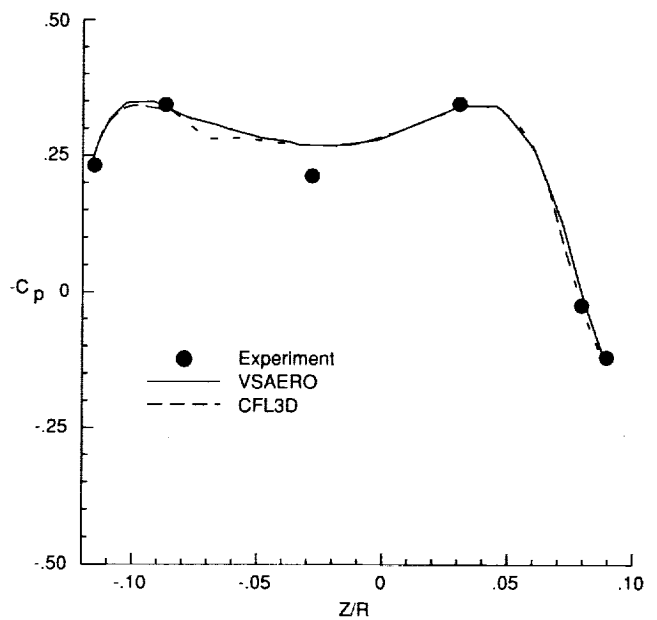
(a) Station $X/R = 0.0517$.



(b) Station $X/R = 0.0941$.

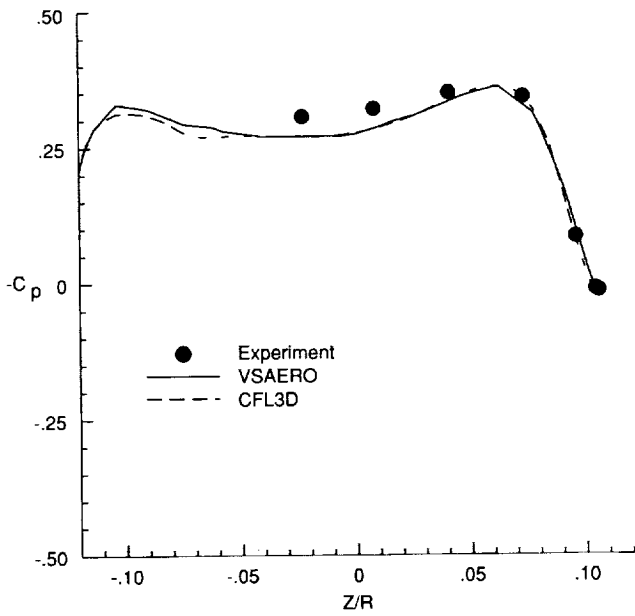


(c) Station $X/R = 0.145$.

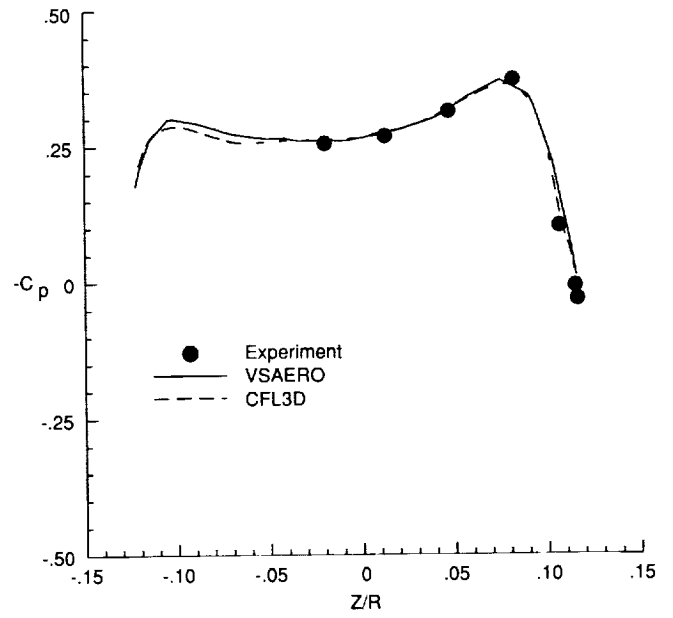


(d) Station $X/R = 0.2007$.

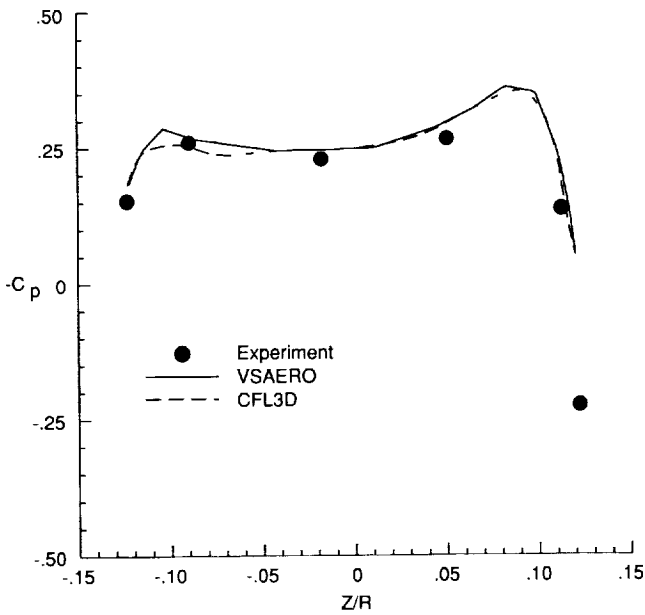
Figure 3. Pressure coefficients. $\alpha = -10^\circ$; $N_{Re} = 4.46 \times 10^6$; $M_\infty = 0.062$.



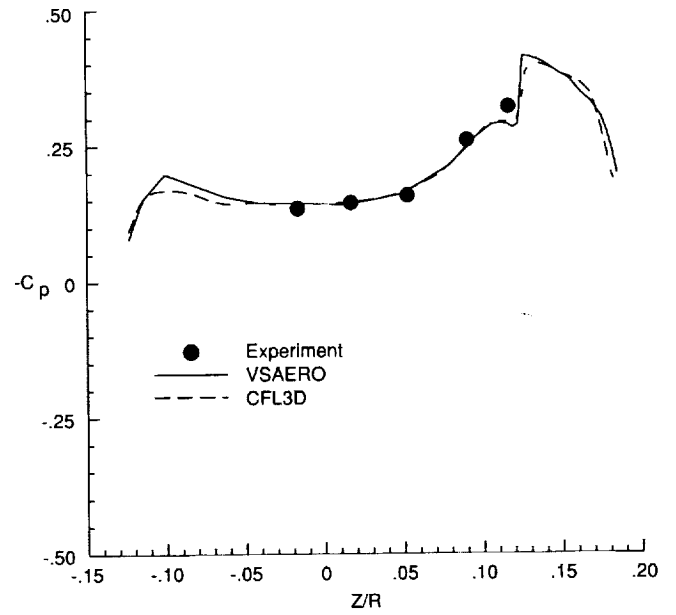
(e) Station $X/R = 0.2563$.



(f) Station $X/R = 0.3074$.

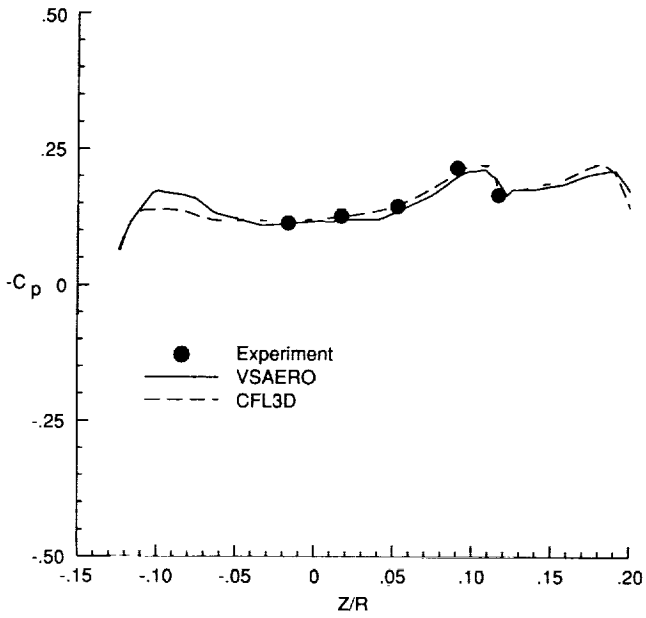


(g) Station $X/R = 0.3497$.

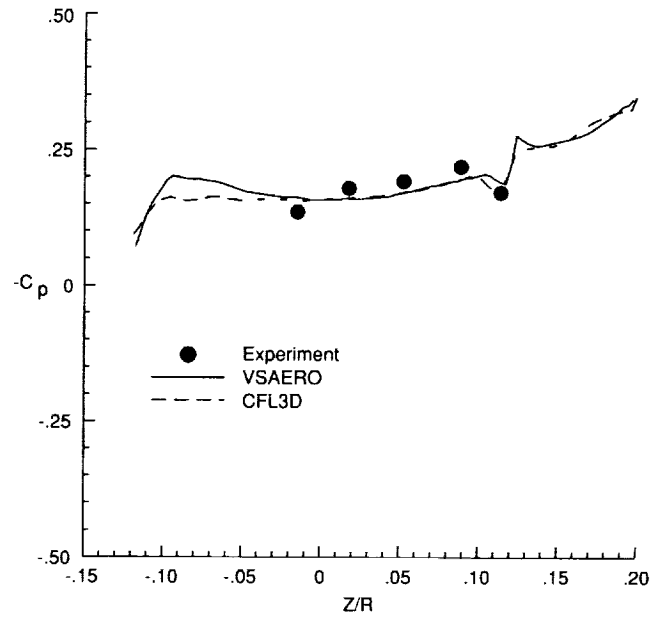


(h) Station $X/R = 0.4669$.

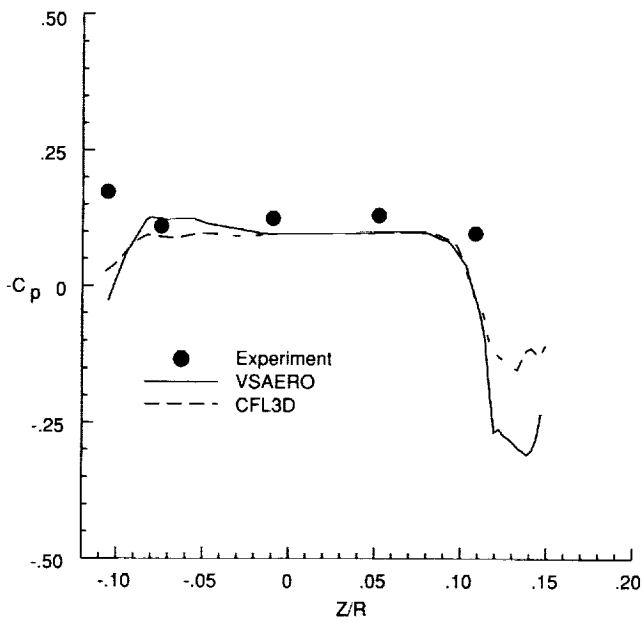
Figure 3. Continued.



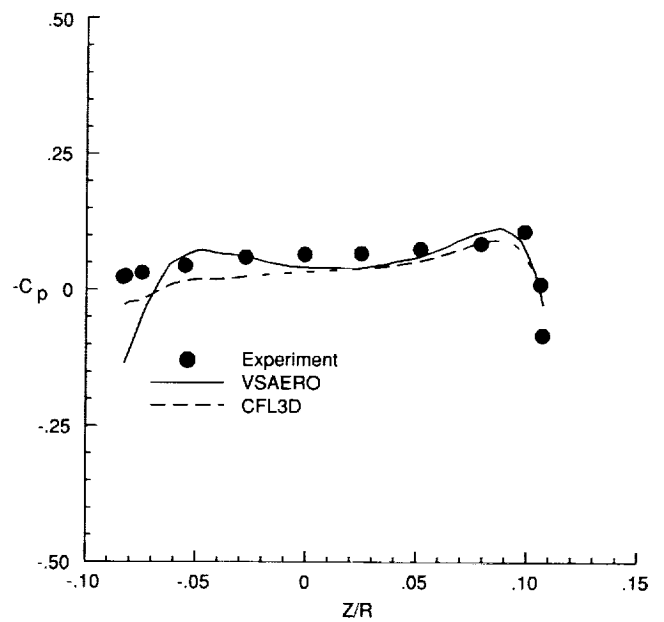
(i) Station $X/R = 0.6003$.



(j) Station $X/R = 0.8809$.

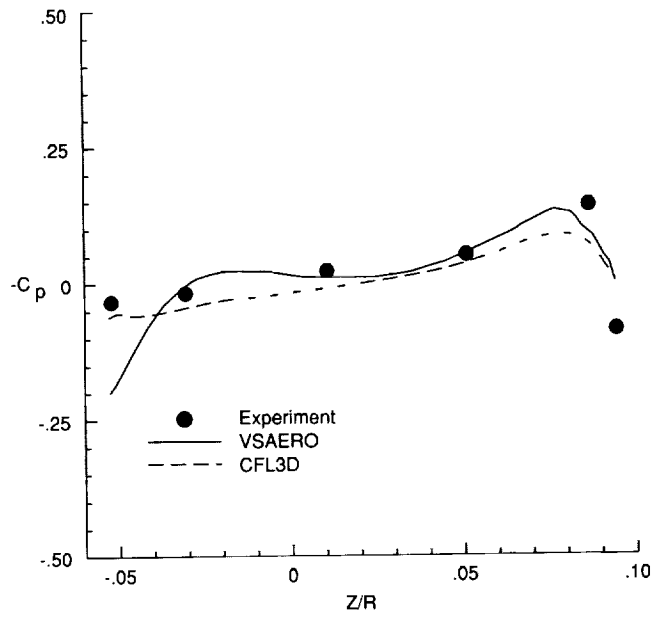


(k) Station $X/R = 1.0008$.

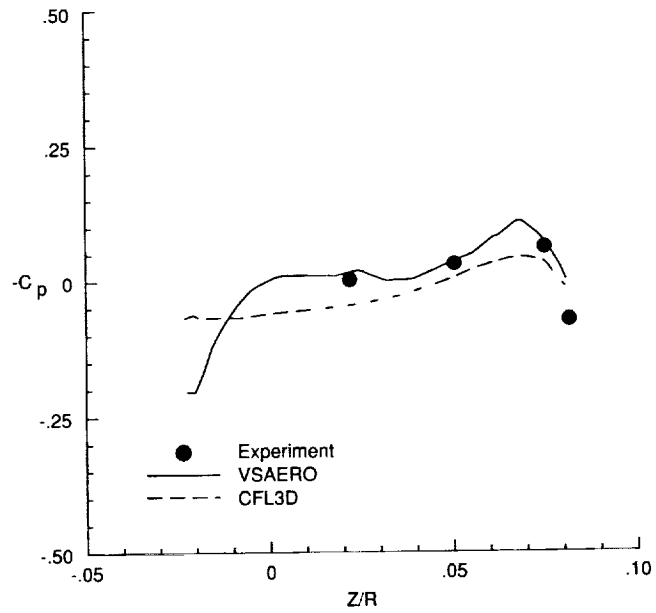


(l) Station $X/R = 1.162$.

Figure 3. Continued.

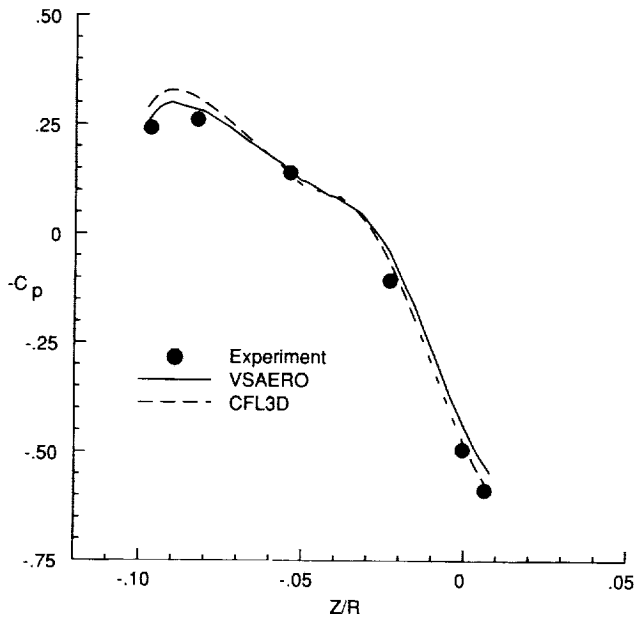


(m) Station $X/R = 1.345$.

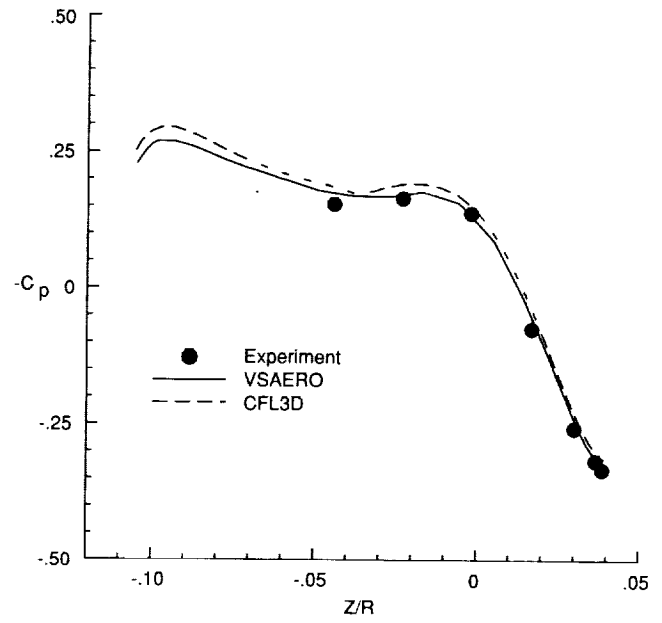


(n) Station $X/R = 1.5298$.

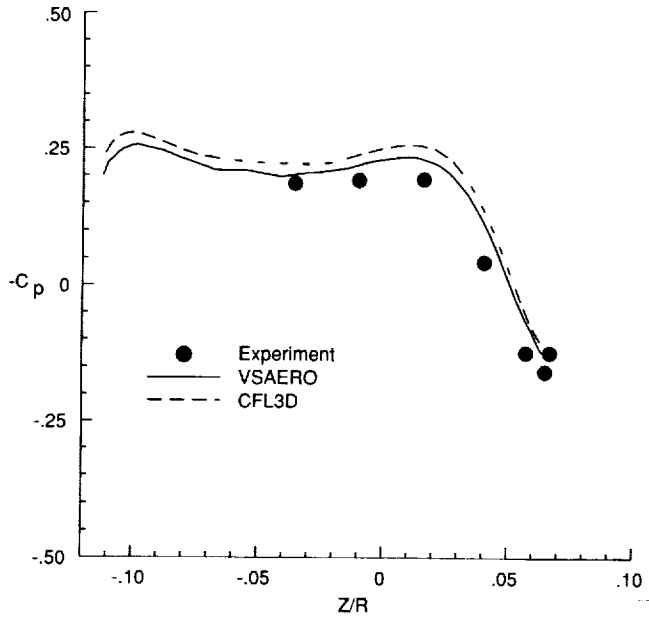
Figure 3. Concluded.



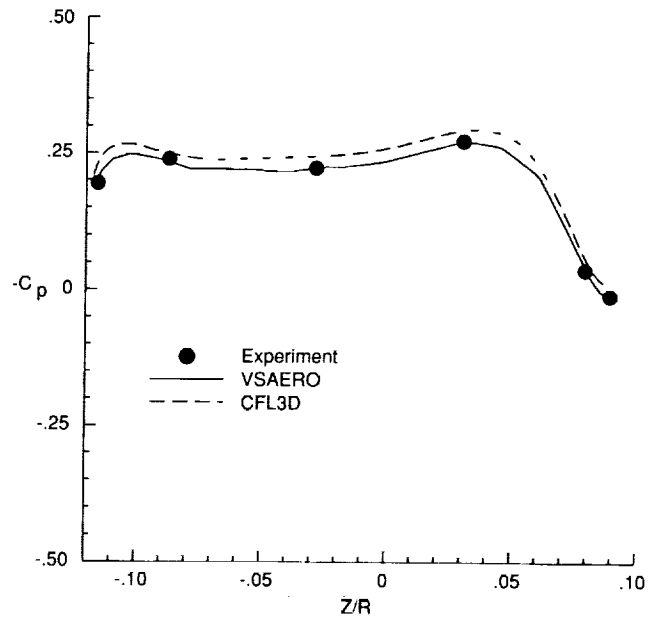
(a) Station $X/R = 0.0517$.



(b) Station $X/R = 0.0941$.

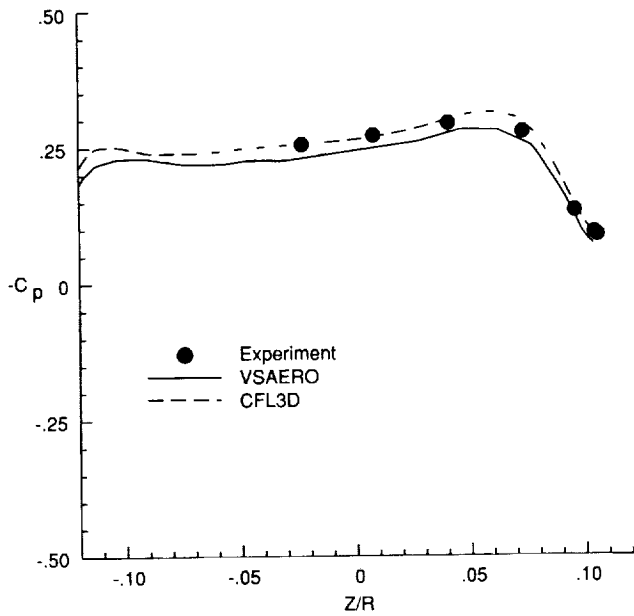


(c) Station $X/R = 0.145$.

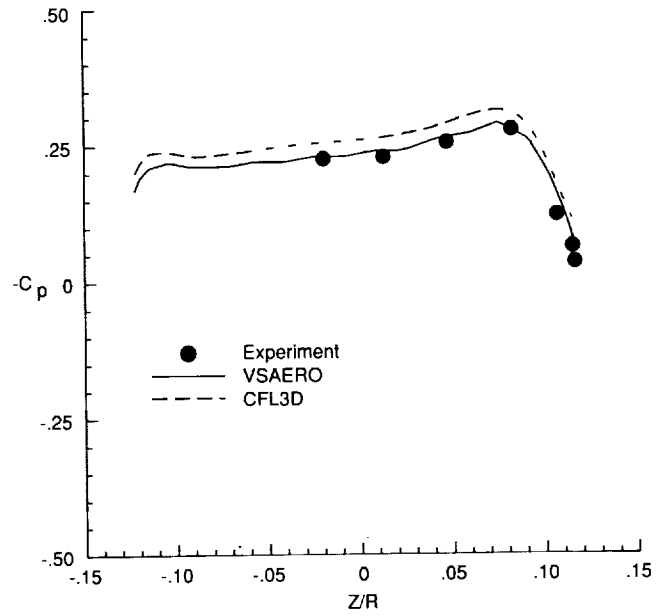


(d) Station $X/R = 0.2007$.

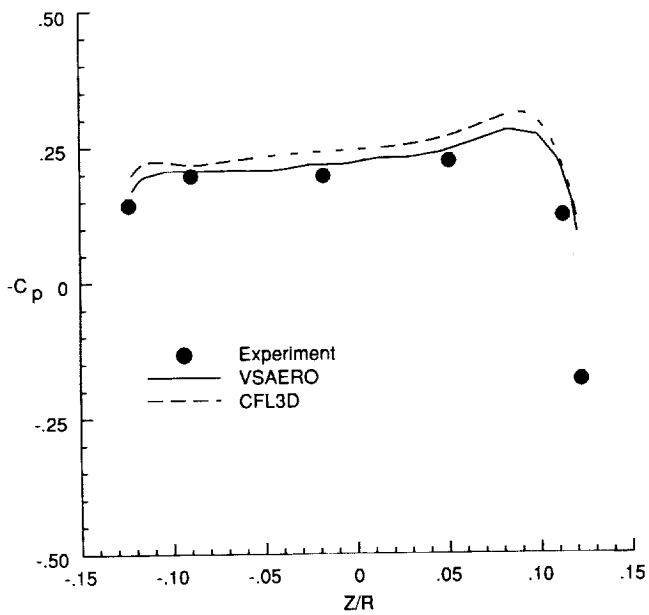
Figure 4. Pressure coefficients. $\alpha = -5^\circ$; $N_{Re} = 4.46 \times 10^6$; $M_\infty = 0.062$.



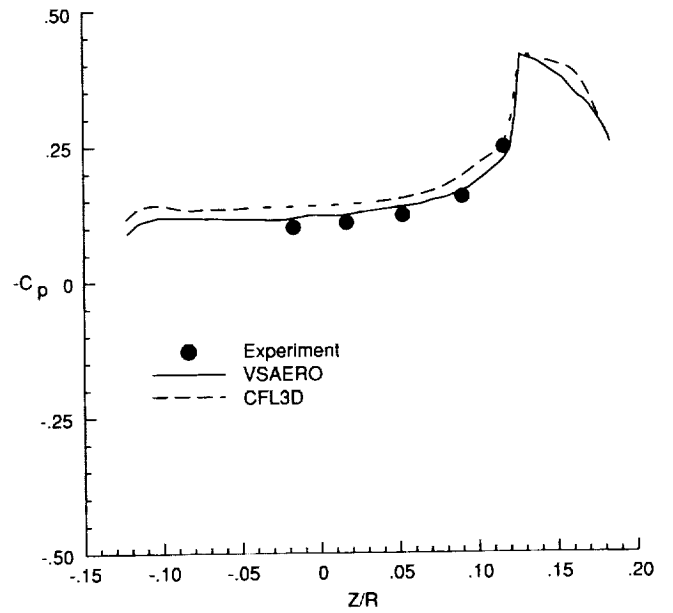
(e) Station $X/R = 0.2563$.



(f) Station $X/R = 0.3074$.

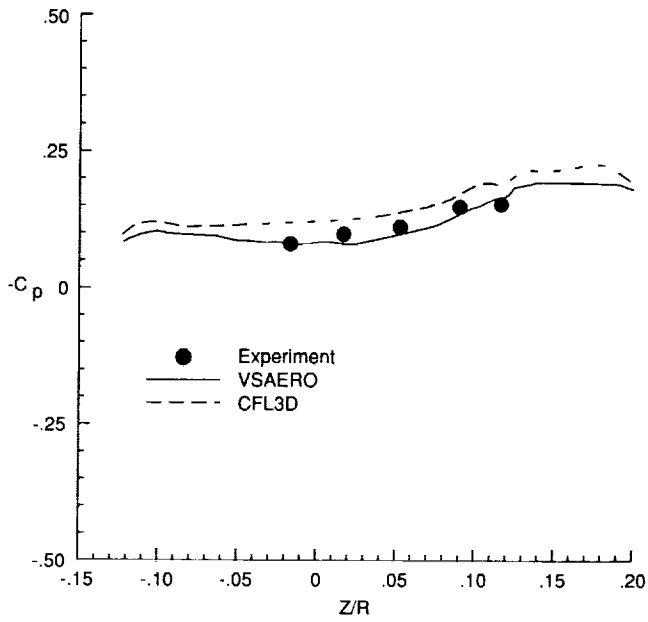


(g) Station $X/R = 0.3497$.

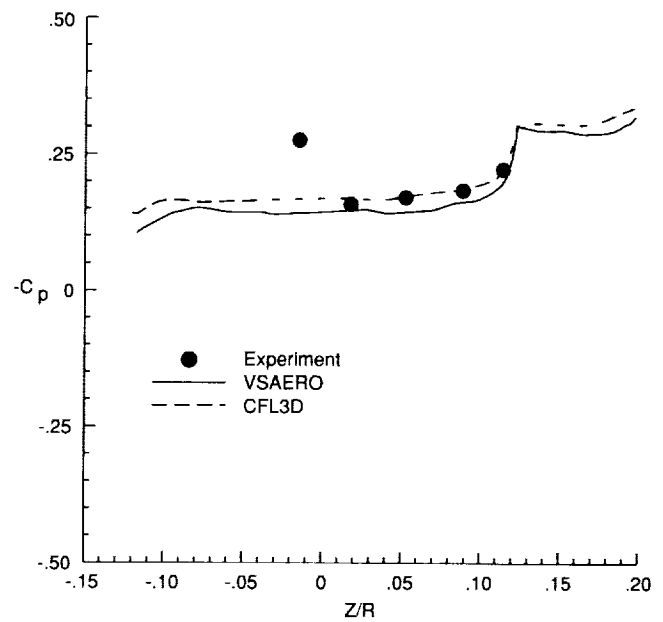


(h) Station $X/R = 0.4669$.

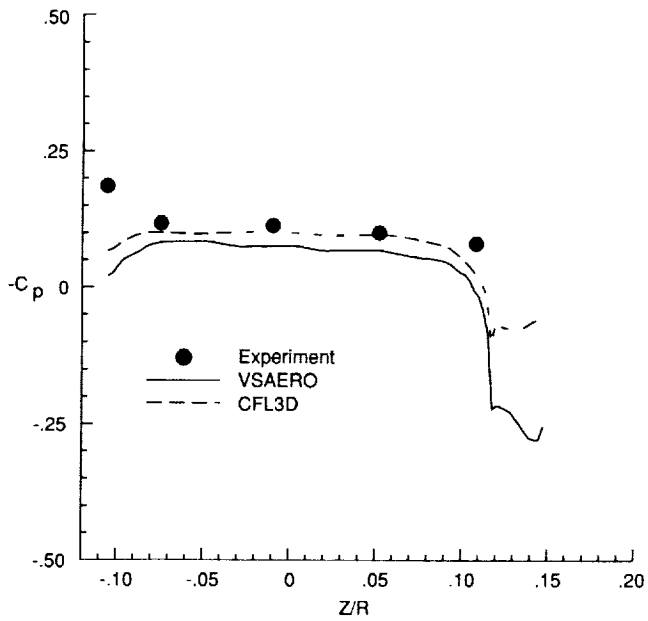
Figure 4. Continued.



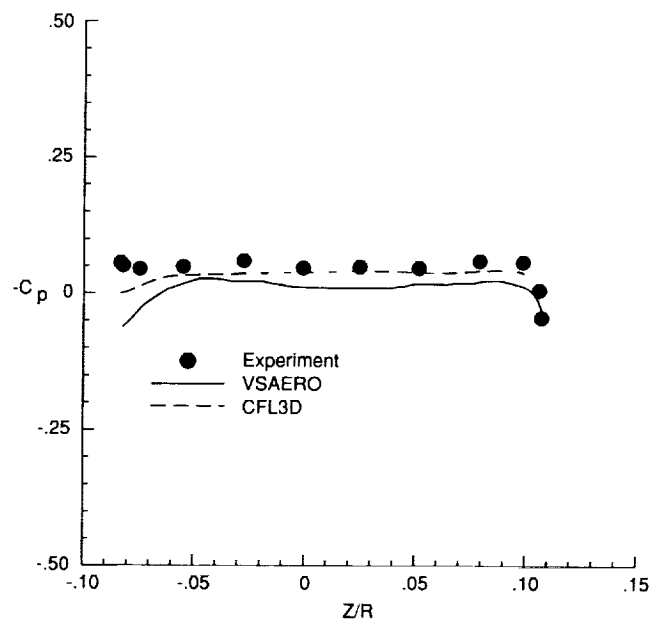
(i) Station $X/R = 0.6003$.



(j) Station $X/R = 0.8809$.

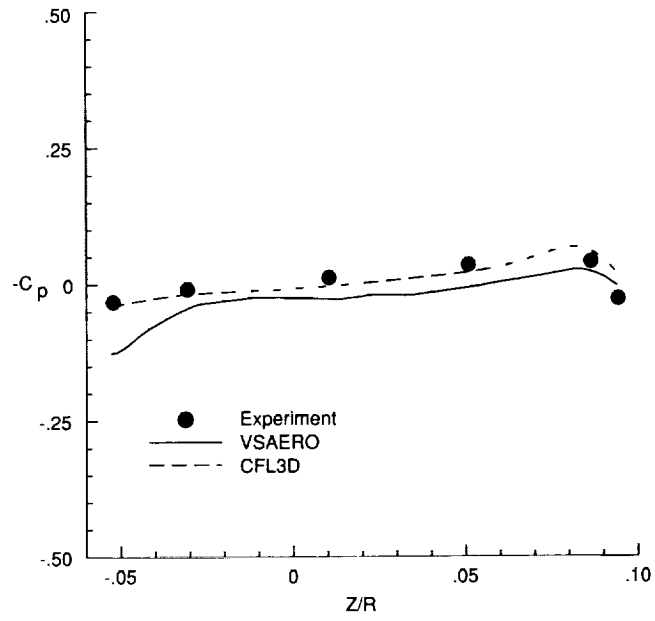


(k) Station $X/R = 1.0008$.

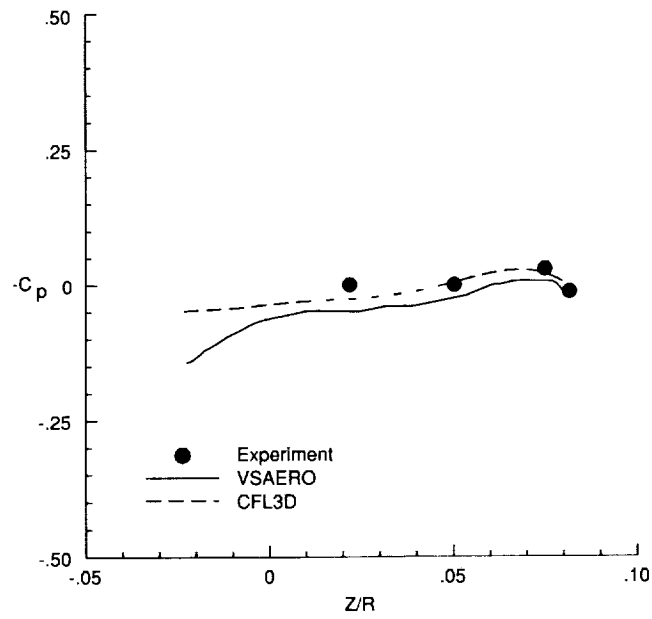


(l) Station $X/R = 1.162$.

Figure 4. Continued.

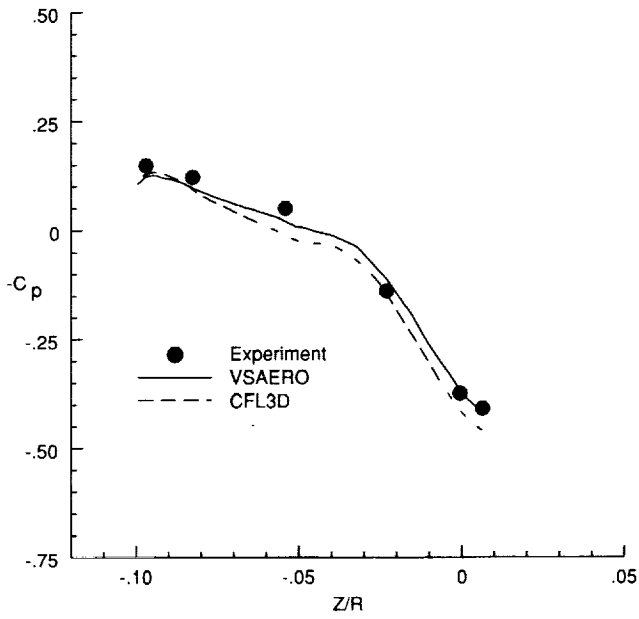


(m) Station $X/R = 1.345$.

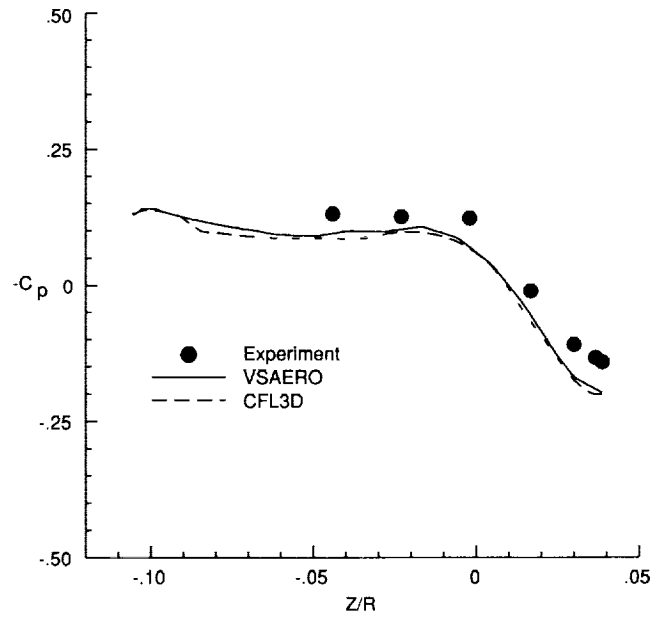


(n) Station $X/R = 1.5298$.

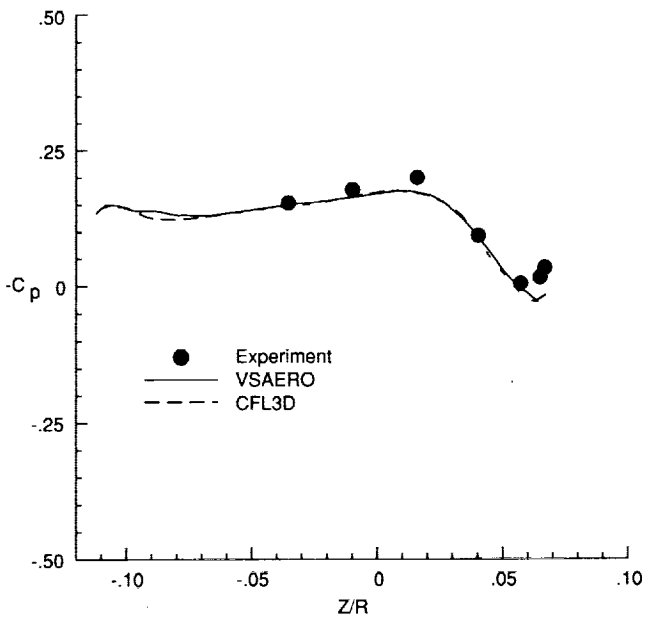
Figure 4. Concluded.



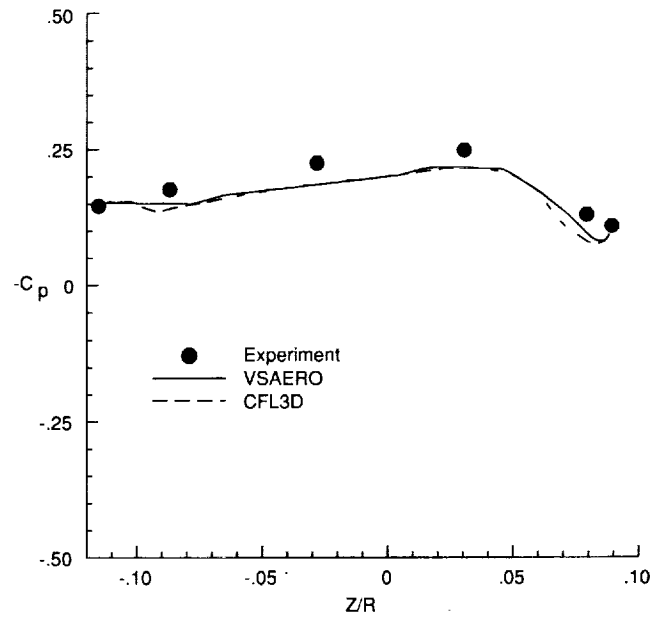
(a) Station $X/R = 0.0517$.



(b) Station $X/R = 0.0941$.

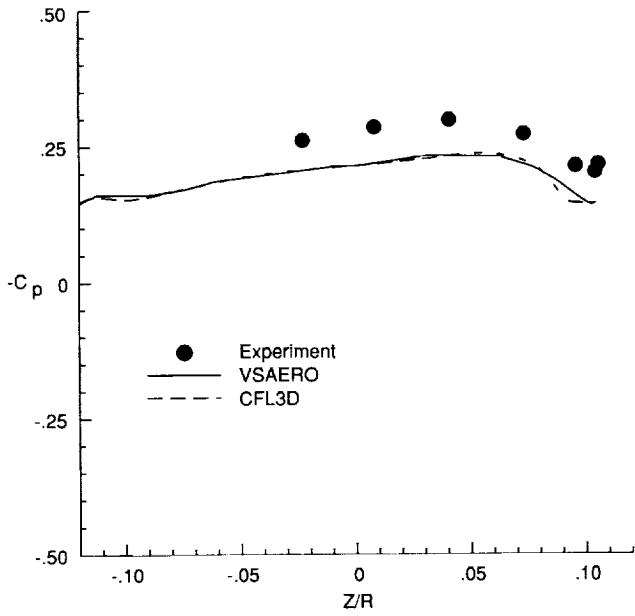


(c) Station $X/R = 0.145$.

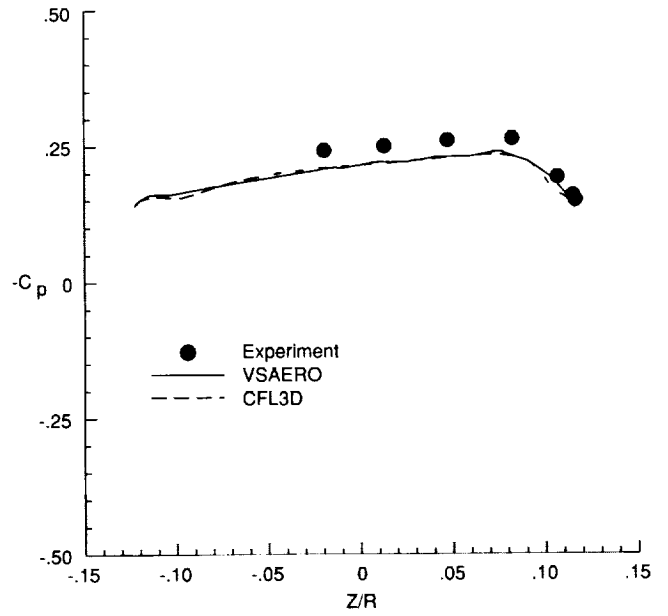


(d) Station $X/R = 0.2007$.

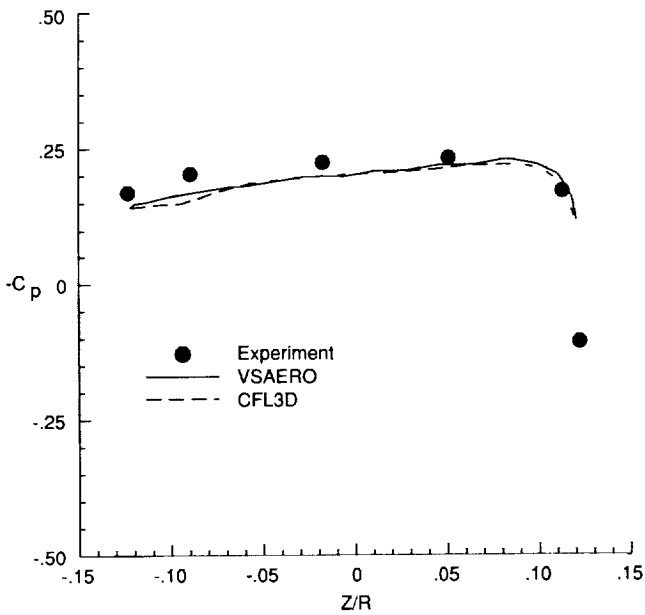
Figure 5. Pressure coefficients. $\alpha = 0^\circ$; $N_{Re} = 4.46 \times 10^6$; $M_\infty = 0.062$.



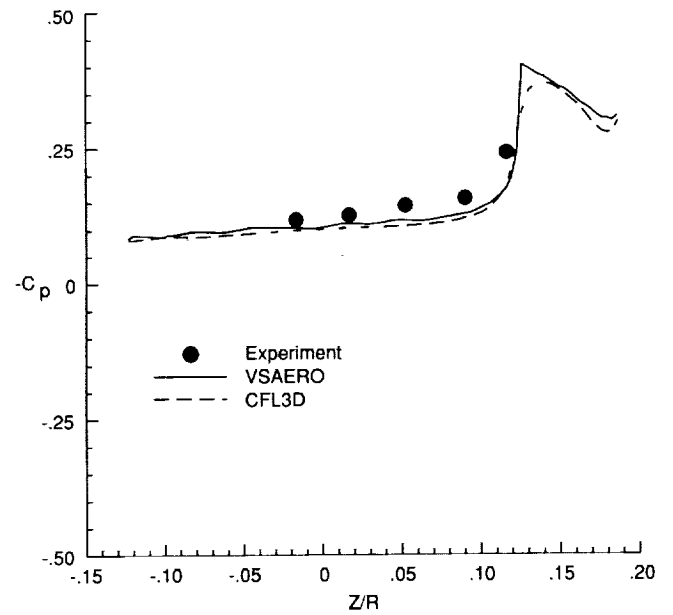
(e) Station $X/R = 0.2563$.



(f) Station $X/R = 0.3074$.

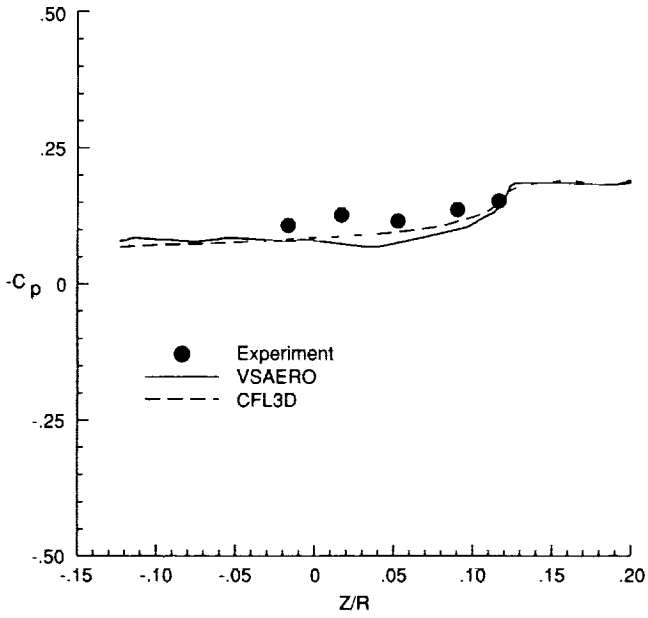


(g) Station $X/R = 0.3497$.

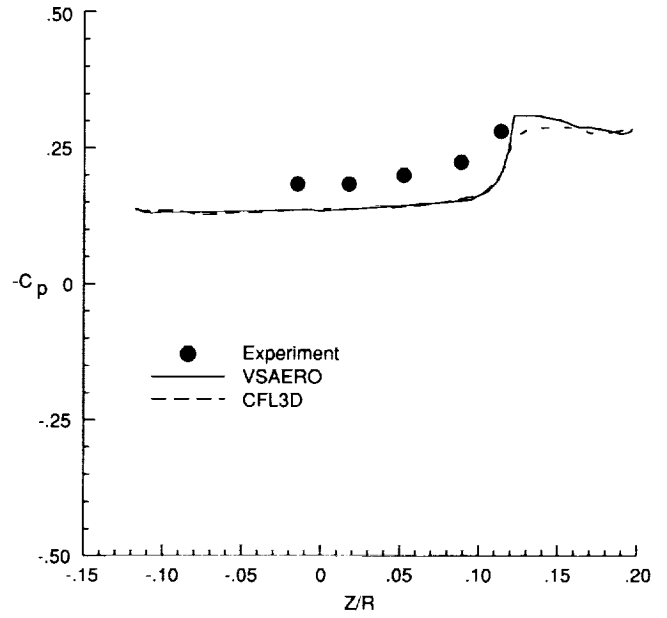


(h) Station $X/R = 0.4669$.

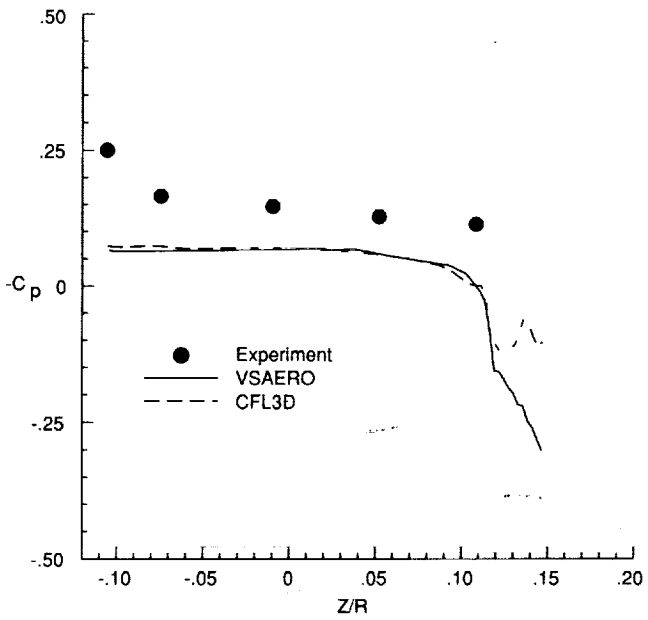
Figure 5. Continued.



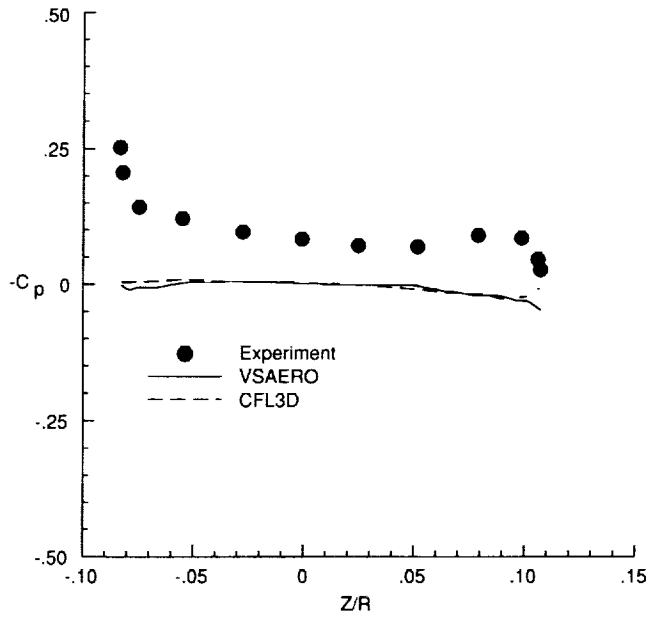
(i) Station $X/R = 0.6003$.



(j) Station $X/R = 0.8809$.

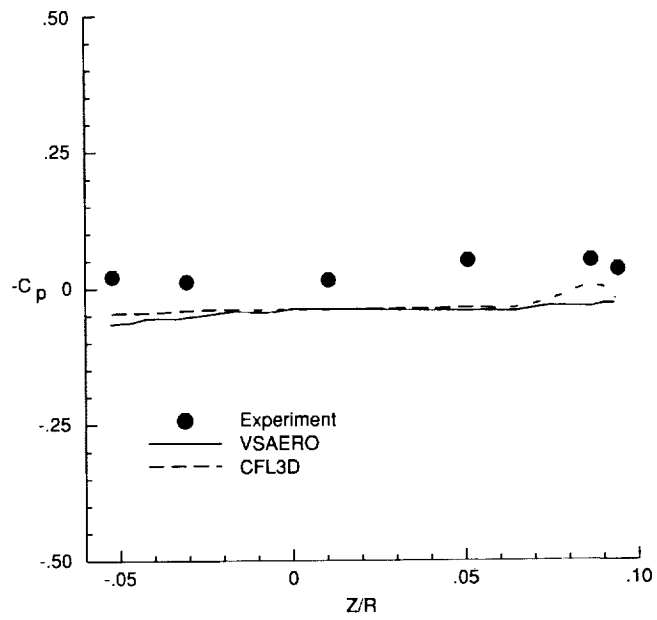


(k) Station $X/R = 1.0008$.

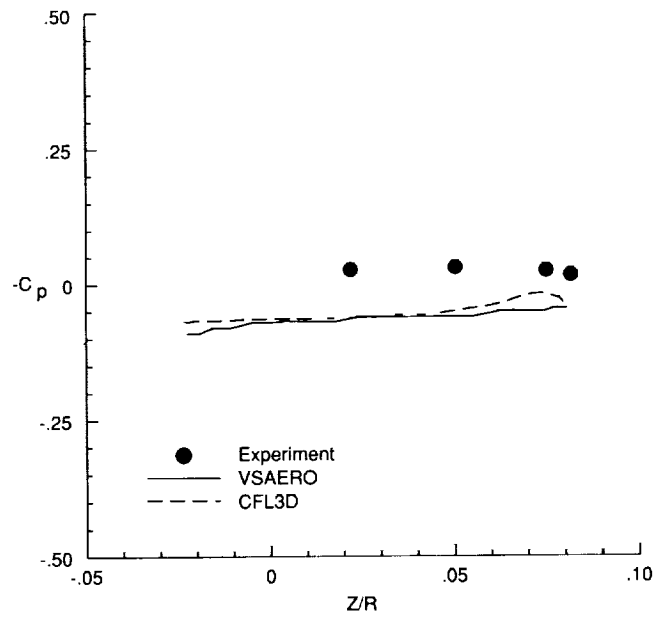


(l) Station $X/R = 1.162$.

Figure 5. Continued.

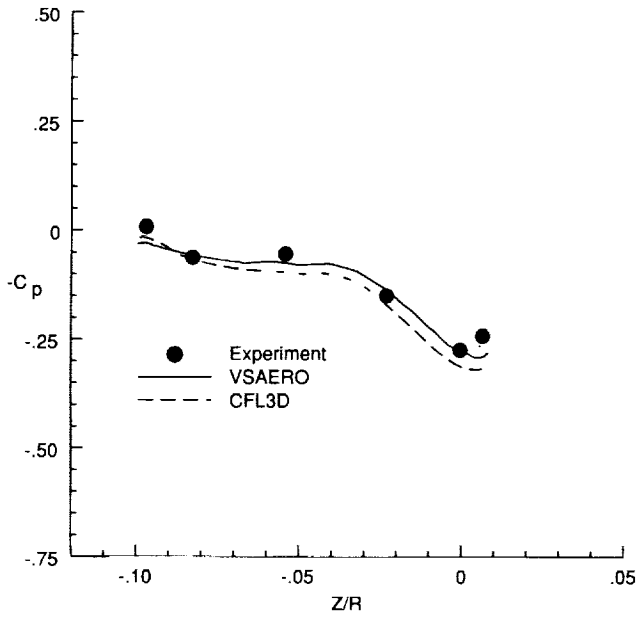


(m) Station $X/R = 1.345$.

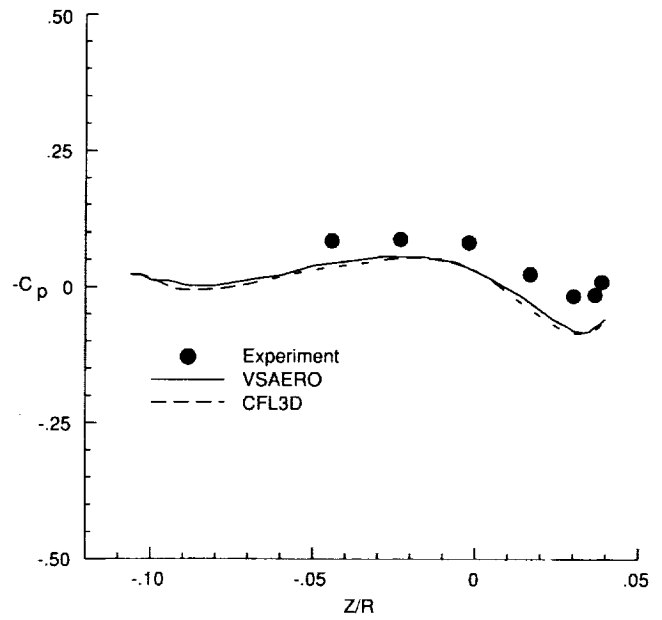


(n) Station $X/R = 1.5298$.

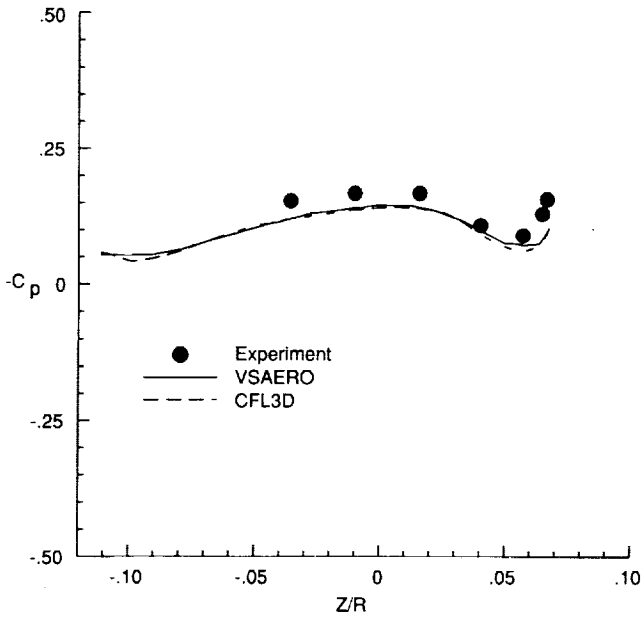
Figure 5. Concluded.



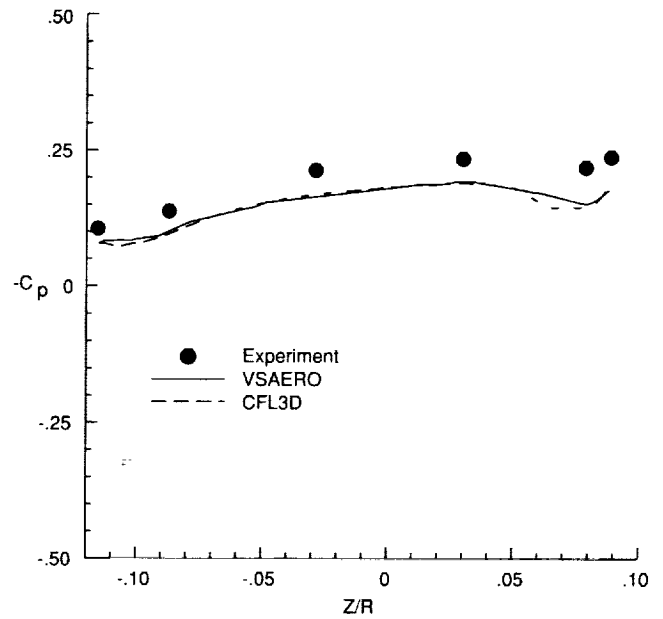
(a) Station $X/R = 0.0517$.



(b) Station $X/R = 0.0941$.

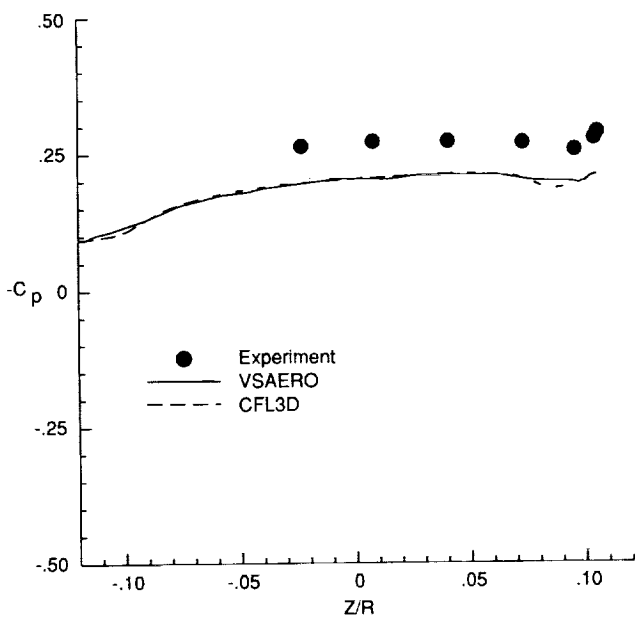


(c) Station $X/R = 0.145$.

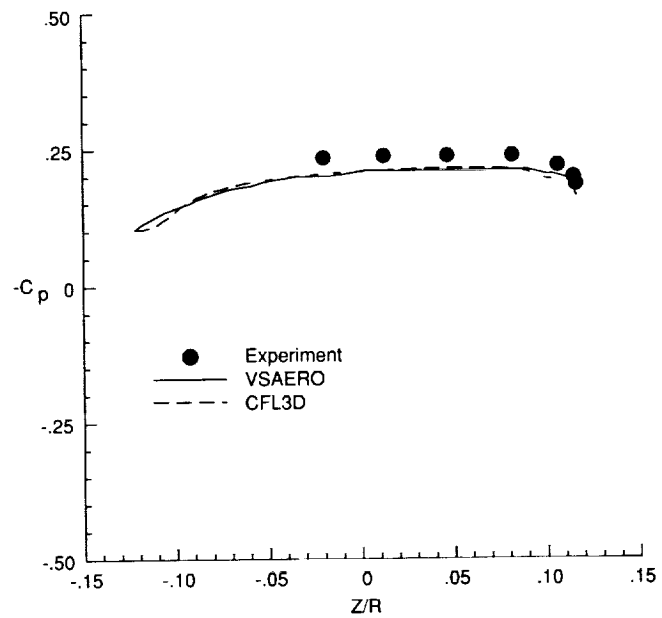


(d) Station $X/R = 0.2007$.

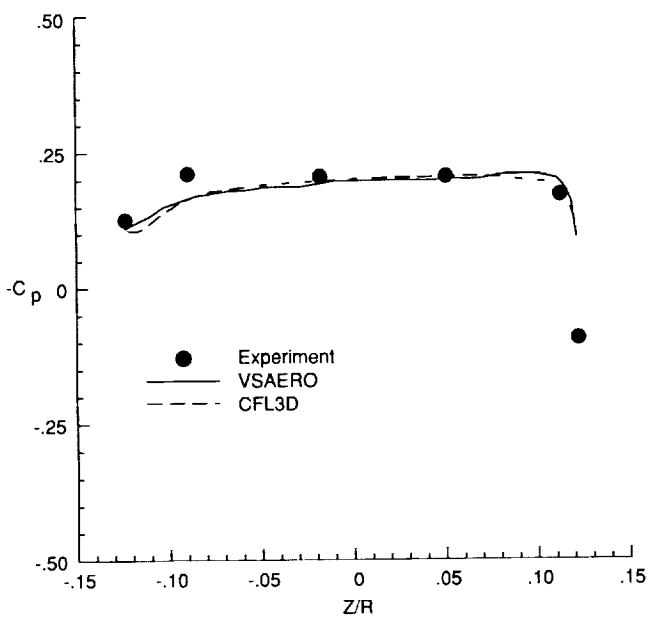
Figure 6. Pressure coefficients. $\alpha = 5^\circ$; $N_{Re} = 4.46 \times 10^6$; $M_\infty = 0.062$.



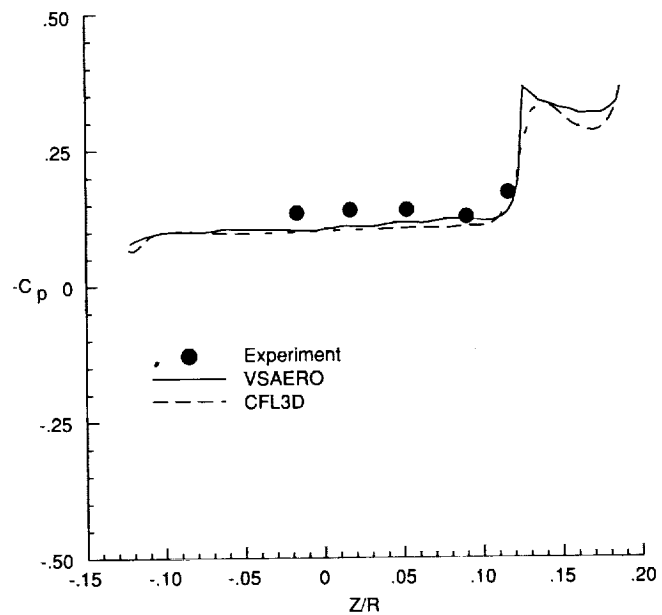
(e) Station $X/R = 0.2563$.



(f) Station $X/R = 0.3074$.

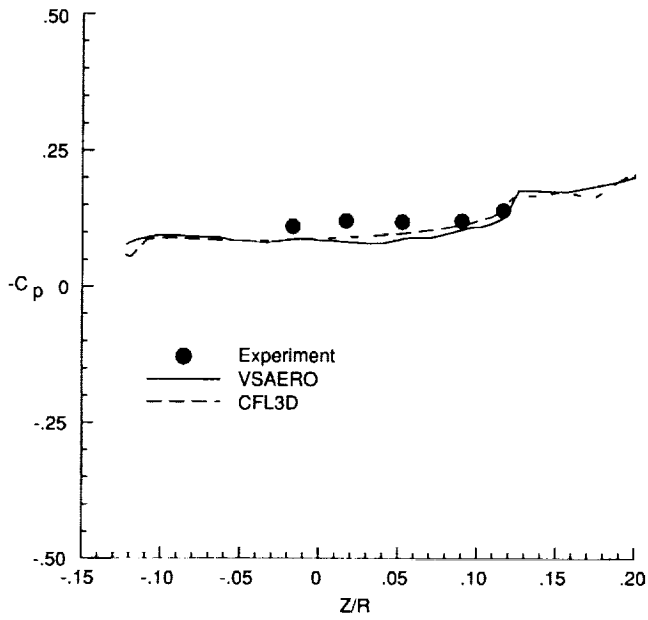


(g) Station $X/R = 0.3497$.

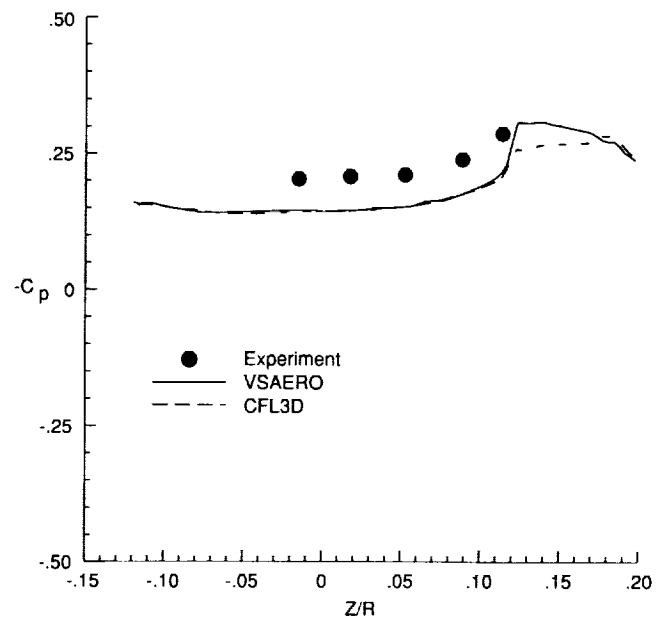


(h) Station $X/R = 0.4669$.

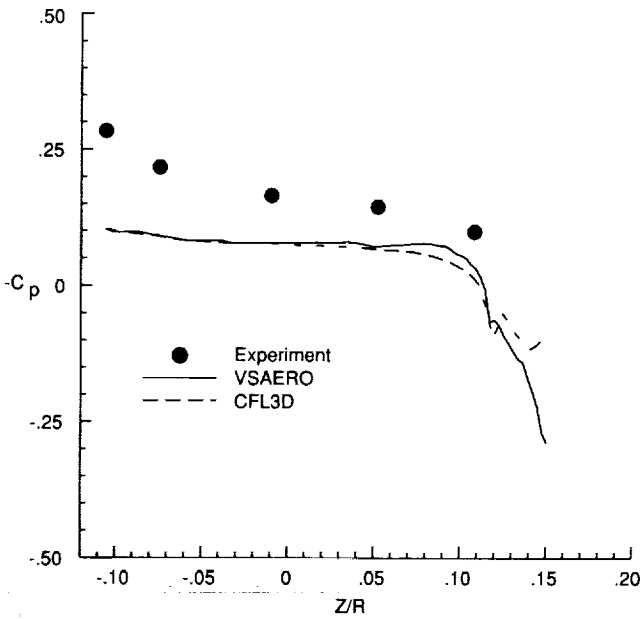
Figure 6. Continued.



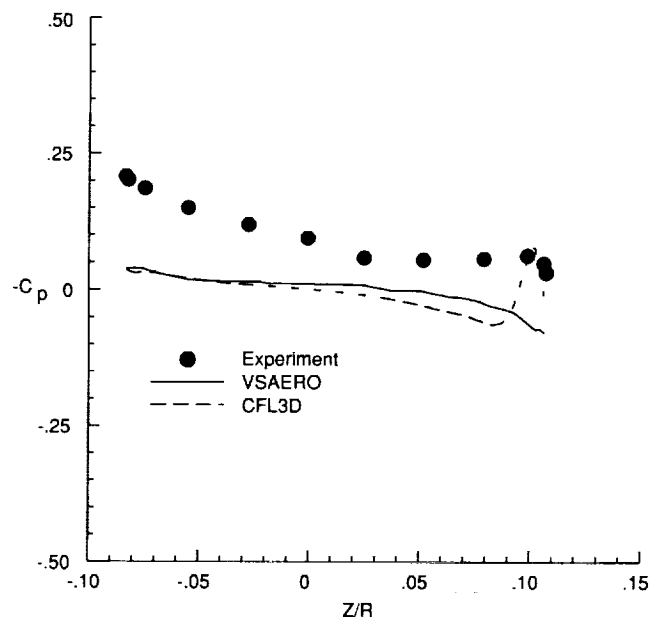
(i) Station $X/R = 0.6003$.



(j) Station $X/R = 0.8809$.

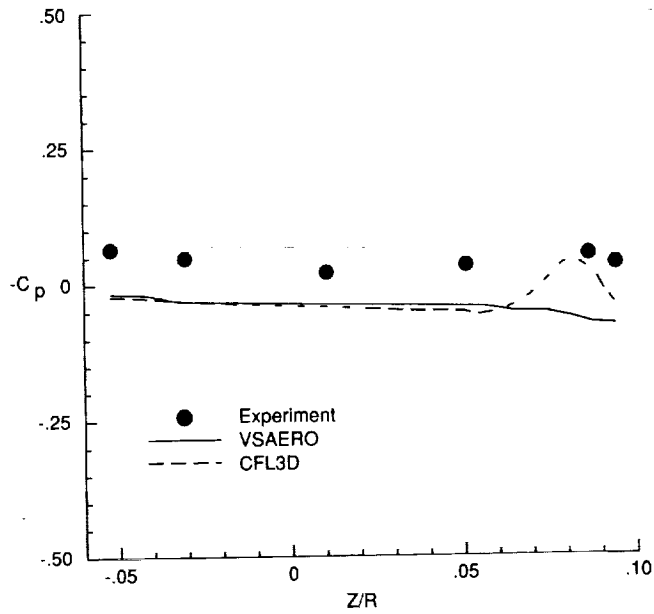


(k) Station $X/R = 1.0008$.

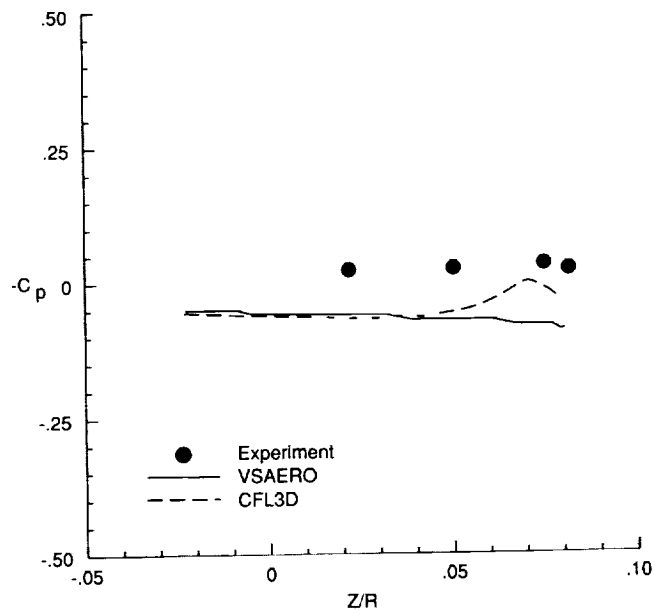


(l) Station $X/R = 1.162$.

Figure 6. Continued.

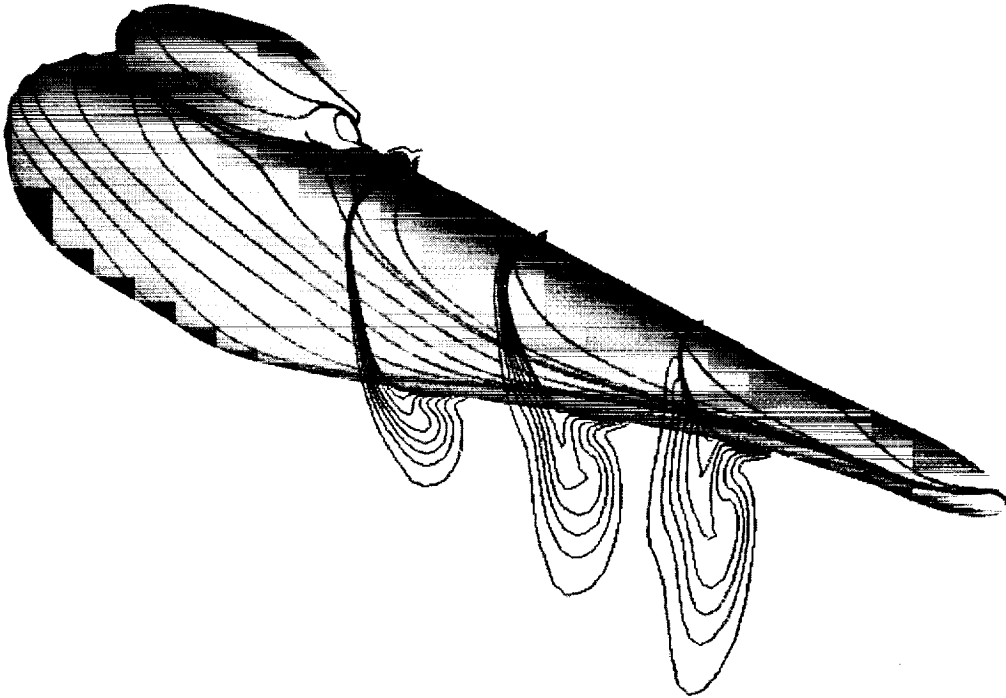


(m) Station $X/R = 1.345$.

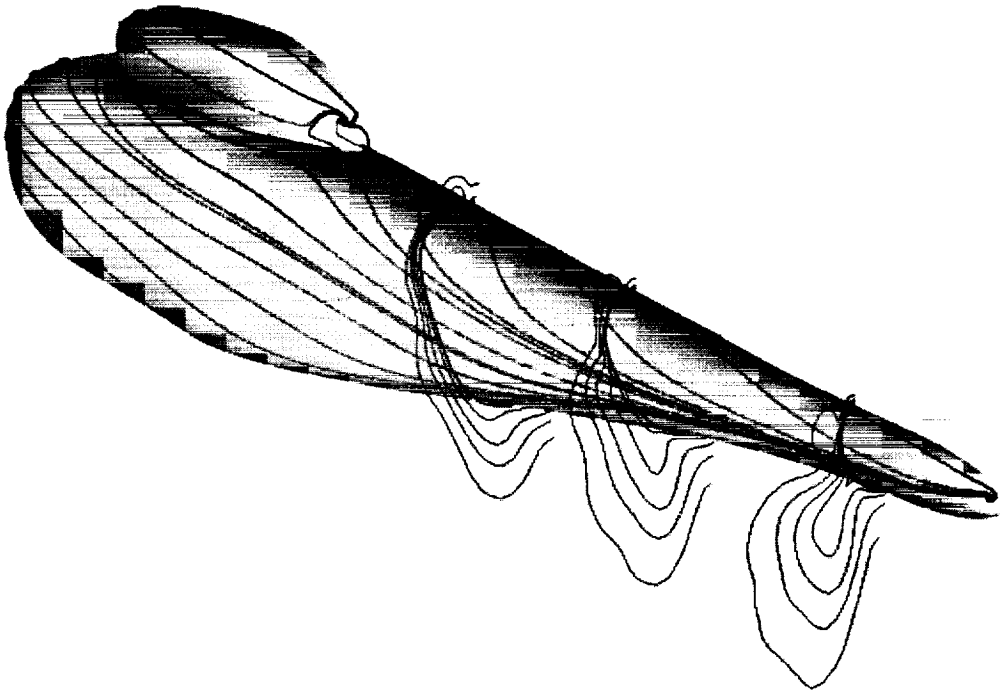


(n) Station $X/R = 1.5298$.

Figure 6. Concluded.

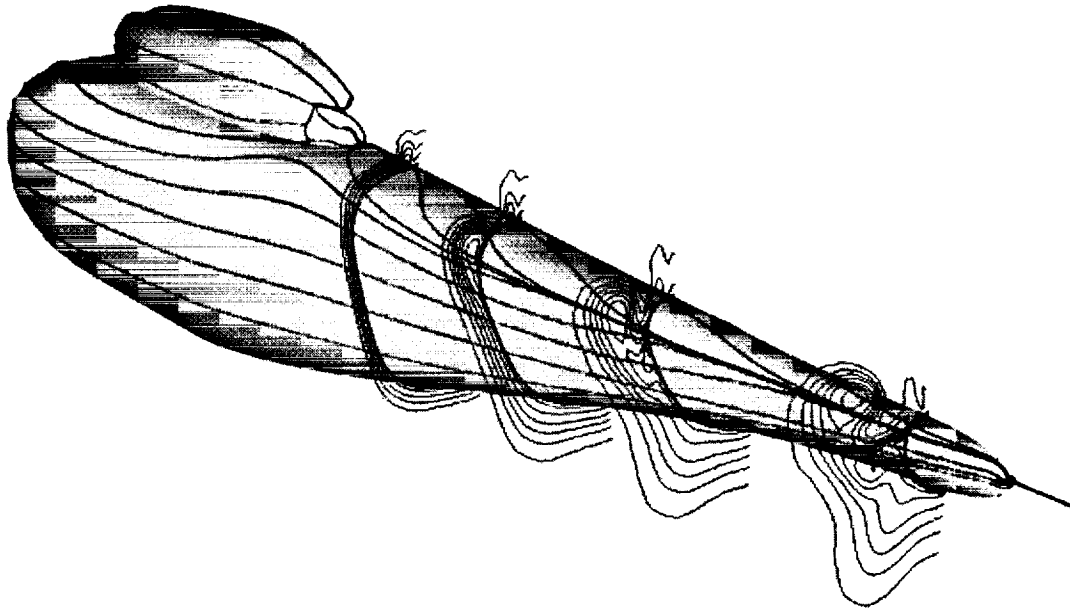


(a) $\alpha = -10^\circ$; $N_{Re} = 4.46 \times 10^6$; $M_\infty = 0.062$.

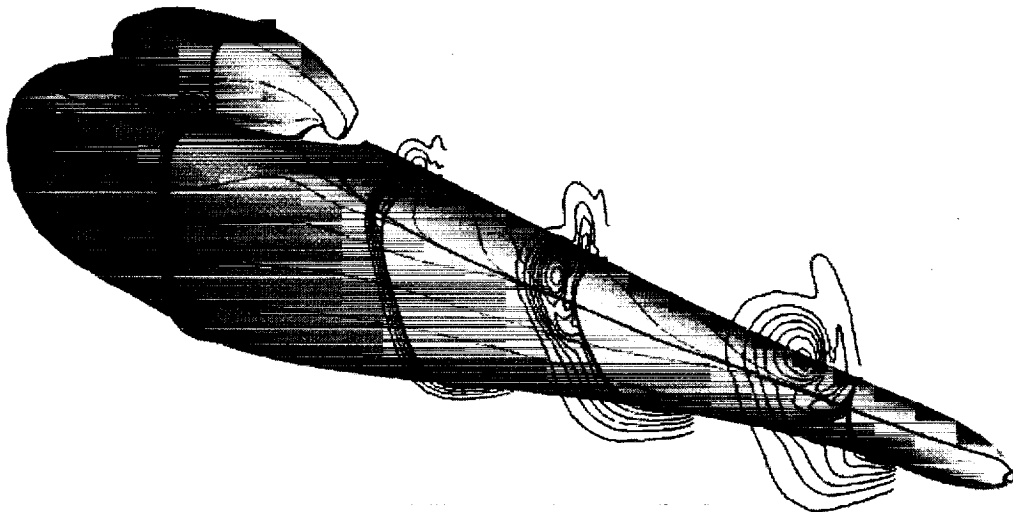


(b) $\alpha = -5^\circ$; $N_{Re} = 4.46 \times 10^6$; $M_\infty = 0.062$.

Figure 7. Surface streamlines and normalized stagnation-pressure contours.

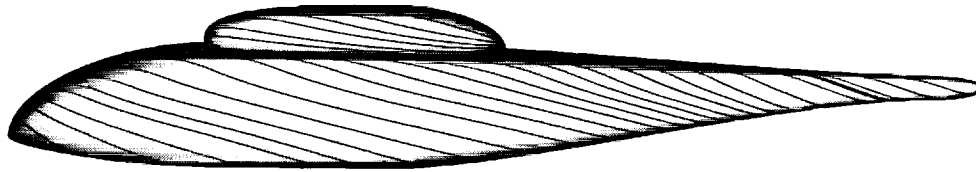


(c) $\alpha = 0^\circ$; $N_{Re} = 4.46 \times 10^6$; $M_\infty = 0.062$.

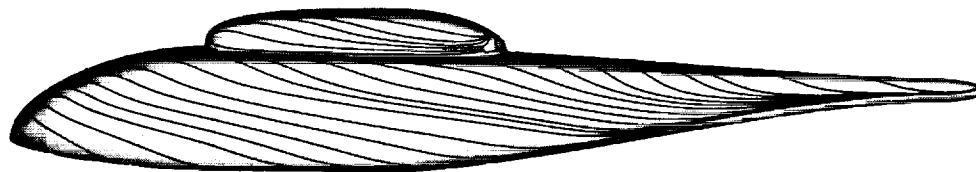


(d) $\alpha = 5^\circ$; $N_{Re} = 4.46 \times 10^6$; $M_\infty = 0.062$.

Figure 7. Concluded.

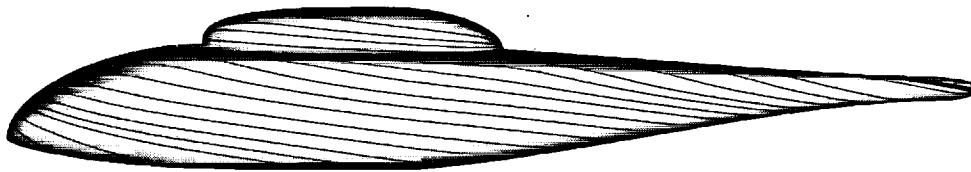


VSAERO

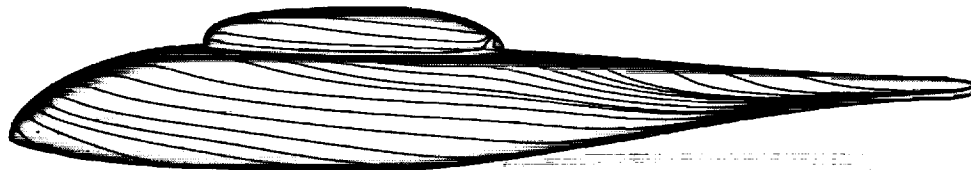


CFL3D

(a) $\alpha = -10^\circ$; $N_{Re} = 4.46 \times 10^6$; $M_\infty = 0.062$.



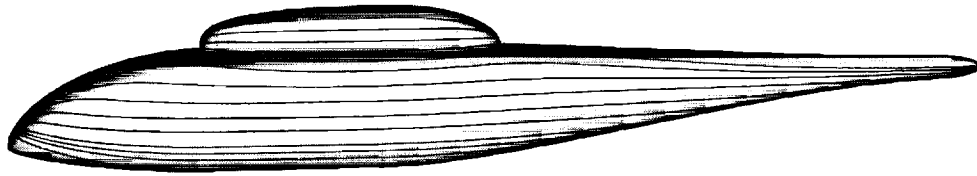
VSAERO



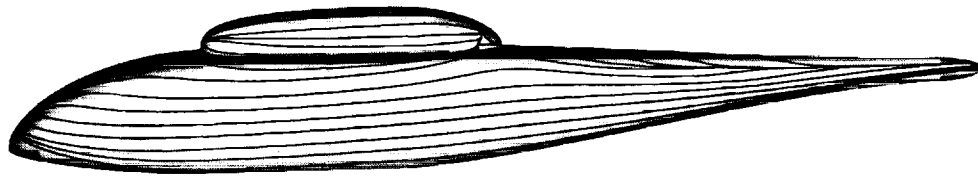
CFL3D

(b) $\alpha = -5^\circ$; $N_{Re} = 4.46 \times 10^6$; $M_\infty = 0.062$.

Figure 8. Surface streamlines.

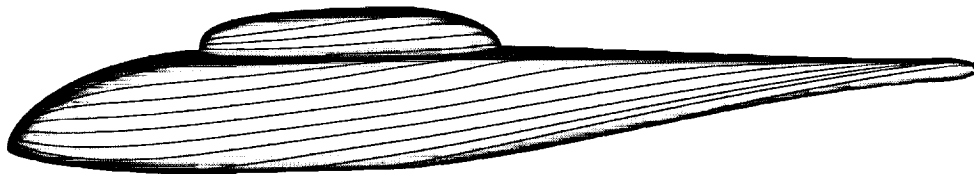


VSAERO

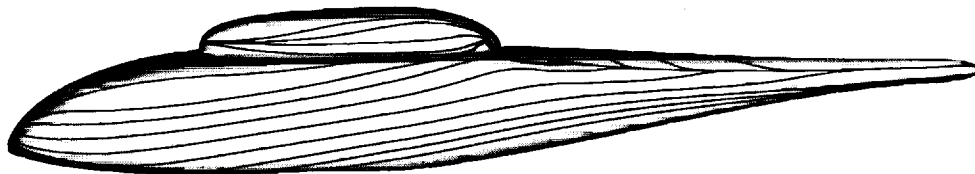


CFL3D

(c) $\alpha = 0^\circ$; $N_{Re} = 4.46 \times 10^6$; $M_\infty = 0.062$.



VSAERO



CFL3D

(d) $\alpha = 5^\circ$; $N_{Re} = 4.46 \times 10^6$; $M_\infty = 0.062$.

Figure 8. Concluded.





